1 **An Analysis of AERONET Aerosol Absorption Properties and Classifications**

2 **Representative of Aerosol Source Regions**

3

4 D. M. Giles,[1,2,3] B. N. Holben,[2] T. F. Eck,[2,4] A. Sinyuk,[1,2] A. Smirnov,[1,2] I. Slutsker,[1,2] R. R.

5 Dickerson,[3] A. M. Thompson,[5] and J. S. Schafer[1,2]

6

7 1. Sigma Space Corporation, Lanham, MD 20706 USA

8 2. Biospheric Sciences Laboratory, NASA Goddard Space Flight Center, Greenbelt, MD 20771

9 USA

10 3. Department of Atmospheric and Oceanic Science, The University of Maryland, College Park,

11 MD 20742 USA

12 4. Universities Space Research Association, Columbia, MD 21044 USA

13 5. Department of Meteorology, The Pennsylvania State University, University Park, PA 16802

14 USA

15
16

17

20   **Abstract**

21   Partitioning of mineral dust, pollution, smoke, and mixtures using remote sensing

22   techniques can help improve accuracy of satellite retrievals and assessments of the aerosol

23   radiative impact on climate. Spectral aerosol optical depth (τ) and single scattering albedo (ω_o)

24   from Aerosol Robotic Network (AERONET) measurements are used to form absorption [i.e., ω_o

25   and absorption Ångström exponent (α_{abs})] and size [i.e., extinction Ångström exponent (α_{ext}) and

26   fine mode fraction of τ] relationships to infer dominant aerosol types. Using the long-term

27   AERONET data set (1999-2010), 19 sites are grouped by aerosol type based on known source

28   regions to: (1) determine the average ω_o and α_{abs} at each site (expanding upon previous work);

29   (2) perform a sensitivity study on α_{abs} by varying the spectral ω_o; and (3) test the ability of each

30   absorption and size relationship to distinguish aerosol types. The spectral ω_o averages indicate

31   slightly more aerosol absorption (i.e., a $0.0<\delta\omega_o\leq0.02$ decrease) than in previous work and

32   optical mixtures of pollution and smoke with dust show stronger absorption than dust alone.

33   Frequency distributions of α_{abs} show significant overlap among aerosol type categories and at

34   least 10% of the α_{abs} retrievals in each category are below 1.0. Perturbing the spectral ω_o by

35   ±0.03 induces significant α_{abs} changes from the unperturbed value by at least ~±0.6 for Dust,

36   ~±0.2 for Mixed, and ~±0.1 for Urban/Industrial and Biomass Burning. The ω_{o440nm} and $\alpha_{ext440-}$

37    $_{870nm}$ relationship shows the best separation among aerosol type clusters, providing a simple

38   technique for determining aerosol type from surface- and future space-based instrumentation.

39

1.0 Introduction

Particles suspended in the atmosphere are difficult to characterize both temporally and spatially due to their short lifetime and geographically diverse sources. Aerosol mixtures—whether dominated by dust, sulfate, carbon, sea salt, or mixtures of these particles—pose a challenge to satellite and sub-orbital remote sensing techniques when identifying aerosol type [*Jeong and Li* 2005; *Levy et al.*, 2007; *Kalapureddy et al.*, 2009; *Lee et al.*, 2010; *Kahn et al.*, 2010; *Russell et al.*, 2010]. Remote sensing techniques can quantify the aerosol particle size using spectral aerosol optical properties, but inferring aerosol type requires knowledge of the source regions usually obtained through use of ancillary data sets (e.g., back trajectory models, satellite product, electron microscopy) to determine emission sources, transport mechanisms, composition, and morphology. The discrimination of aerosol types increases accuracy of the assessment of the aerosol radiative impact and therefore is important to climate modeling [*Diner et al.*, 1999; *Satheesh and Moorthy* 2005]. Variations in spectral aerosol absorption magnitudes can enable partitioning among aerosols from various source regions, fuel types, or combustion phases. Aerosol absorption together with size can potentially determine dominant aerosol type from remote sensing and in situ measurements.

Various methods have been proposed using aerosol optical and microphysical properties to distinguish aerosol types. The magnitude of the aerosol optical depth (AOD, τ_{ext}) and the spectral dependence of AOD with respect to wavelength (i.e., Ångström exponent, α_{ext}) is commonly used in aerosol remote sensing to infer dominant aerosol types given knowledge of the source region or typical aerosol transport mechanisms [e.g., *Kalapureddy et al.*, 2009, *Boselli et al.*, 2012]. Other techniques using the derivative of the Ångström exponent or spectral difference of Ångström exponent wavelength pairs along with aerosol loading and particle

3

effective radius may provide further information on particle type with respect to size and growth

of particles [*Gobbi et al*., 2007; *Basart et al.*, 2009]. Although size varies among particle types,

the spectral absorption also varies. Studies [*Omar et al*., 2005, *Levy et al*., 2007; *Mielonen et al*.,

2009; *Lee et al*., 2010; *Russell et al*., 2010] have suggested relationships utilizing the aerosol

absorption and size properties to determine the dominant aerosol type from Aerosol Robotic

Network (AERONET) retrievals [*Holben et al*., 1998; *Dubovik et al*., 2000; *Dubovik et al*., 2002;

Dubovik et al., 2006]. Information content from these relationships varies from generic

identification of major aerosol particle types (e.g., dust, mixed, urban/industrial pollution, and

biomass burning smoke) to specific degrees of absorbing aerosols. Recently, *Russell et al.*

[2010] have proposed using the absorption Ångström exponent (AAE, α_{abs}), the spectral

absorption aerosol optical depth dependence on wavelength, to further define aerosol type from

AERONET retrievals. For comparison to the Cloud-Aerosol Lidar with Orthogonal Polarization

(CALIOP) instrument, *Mielonen et al.* [2009] utilized the AERONET single scattering albedo

(ω_o) difference between 440 and 1020 nm (as suggested by *Bergstrom et al.* [2002] and

implemented by *Derimian et al.* [2008]) and α_{ext} to estimate aerosol type. Further, *Lee et al.*

[2010] modified this relationship to use only ω_o from 440 nm and the fine mode fraction (η) of

the AOD at 550 nm to determine the particle size partitioning. Other techniques using spectral

lidar ratios and multiple aerosol optical and microphysical properties retrieved from AERONET

have been implemented to determine aerosol type categories for various applications [*Cattrall et*

al., 2005; *Omar et al*., 2005; *Qin and Mitchell* 2009; *Burton et al*., 2012].

In this study, for data available between 1999 and 2010, 19 AERONET sites were

classified by dominant aerosol type [i.e., Dust, Mixed, Urban/Industrial (U/I), and Biomass

Burning (BB)] based on previous literature. First, aerosol absorption parameters (i.e., ω_o and

86   α_{abs}) were analyzed and compared to previous work. Second, sensitivity tests were performed on

87   the α_{abs} by perturbing ω_o to determine variability within each dominant aerosol type category.

88   Last, the absorption and size relationships were evaluated and compared to each other based on

89   the dominant aerosol type categorizations.

90   **2.0 Instrumentation and Method**

91   The Aerosol Robotic Network is a ground-based network of standardized Cimel Sun and

92   sky scanning radiometers measuring AOD at multiple wavelengths from 340 to 1640 nm and

93   retrieving other columnar optically effective aerosol properties (e.g., volume size distribution,

94   complex index of refraction, and single scattering albedo) from sky radiance measurements at

95   four wavelengths: 440, 675, 870, and 1020 nm [*Holben et al*., 1998]. The AOD estimated

96   uncertainty varies spectrally from ±0.01 to ±0.02 with the highest error in the ultraviolet

97   wavelengths [*Holben et al*., 1998; *Eck et al*., 1999] and calibrated sky radiance measurements

98   typically have an uncertainty less than 5% [*Holben et al*., 1998]. Further descriptions of the

99   instrumentation, calibration, methodology, data processing, and data quality are described

100 elsewhere [*Holben et al*., 1998; 2006; *Eck et al*., 1999; 2005; *Smirnov et al*., 2000]. For all sky

101 radiance wavelengths (440, 675, 870, and 1020 nm), the ω_o uncertainty is expected to be ±0.03

102 based on Version 1 almucantar retrieval computations when $\tau_{440nm}>0.4$ [*Holben et al.*, 1998; *Eck*

103 *et al*., 1999; *Dubovik et al*., 2002]. When compared to AERONET ω_o retrievals, in situ

104 measurements of ω_o were within AERONET uncertainty estimates [*Leahy et al*., 2007; *Johnson*

105 *et al*., 2009; *Müller et al*., 2010; *Toledano et al*., 2011].

106   In-depth discussions of the almucantar retrieval products are given by *Dubovik and King*

107 [2000] and *Dubovik et al.* [2000; 2002; 2006] and quality criteria are discussed by *Holben et al.*

108   [2006]. *Dubovik et al.* [2002] provided averaged almucantar retrieval aerosol optical and

109   microphysical properties based on aerosol types and source region using AERONET pre-Version

110   1 data (i.e., data collected and analyzed prior to the release of quality assured Version 1 retrieval

111   data set in 2003). These results have been used throughout the literature to define aerosol type

112   based on the aerosol absorption characteristics [*Russell et al.*, 2010 and references therein].

113   Notably, the Version 2 retrievals (i.e., released in 2006) utilized new input data sets (e.g., NCEP

114   reanalysis, MODIS ecosystem type-based BRDF functions, and geographically and temporally

115   varying black sky albedo), more dynamic calculations of the surface reflectance than the Version

116   1 assumption of a green Earth surface reflectance, robust quality checks of the measured sky

117   radiance inputs, and improved criteria for acceptable sky residual fits [*Holben et al.*, 2006; *Leahy*

118   *et al.*, 2007; *Eck et al.*, 2008 and references therein]. For example, in the United Arab Emirates

119   and Arabian Gulf, Version 2 improvements provided more consistent ω_o magnitudes and spectra

120   for coarse-mode dust aerosol over two vastly different surfaces (i.e., small island versus bright

121   desert) with ω_o differences of less than 0.01 compared to 0.03 for the Version 1 spheroid

122   inversion model and with increased absorption at 440 nm, which typically occurs in iron-rich

123   desert dust, rather than spectrally neutral ω_o from Version 1 retrievals [*Eck et al.*, 2008].

124   Additional instrument checks were implemented to assess absorption properties from the

125   Version 2 almucantar retrievals. To improve the quality of the sky radiance measurements used

126   for almucantar retrievals, instrument collimator consistency checks were performed to remove

127   potential artifacts (e.g., induced by spider webs in the tube, excessive dust, or contamination on

128   the sensor head window due to moisture or dust) in the radiance measurements. The sky

129   radiance measurements at $\pm 6°$ azimuth from solar zenith—using the solar aureole and sky gains

130   for instruments with only Silicon detectors—were required to have a percent difference of less

131   than 10% spectrally from 440 to 1020 nm. For Silicon and InGaAs detector instruments (where

132   each detector measures in a different collimator tube), the temperature corrected Silicon and

133   InGaAs $\tau_{1020\,nm}$ difference ($\Delta\tau$) must be less than $\Delta\tau_{limit}$ of 0.06/m (where m is the optical air

134   mass), which results in a $\Delta\tau_{limit}$ of 0.03 when m equals 2 and 0.06 for the overhead sun (m=1).

135   Collimator consistency checks provide an improved method to further quality assure the Level

136   2.0 almucantar retrieval data set.

137   Measured aerosol optical depth and computed almucantar retrieval products can be used

138   to derive additional aerosol properties. The extinction Ångström exponent (α_{ext}) was calculated

139   from the spectral dependence of AOD or τ_{ext} with wavelength (λ) using equation (1) [*Ångström*

140   *1964*]:

$$\alpha_{ext} = -dln[\tau_{ext}(\lambda)]/dln(\lambda) \tag{1}$$

141   For a wavelength range between 440 and 870 nm typically using 440, 500, 675, and 870 nm

142   AOD—and computed by linear regression of ln τ versus ln λ—values near 0 indicate mainly

143   coarse mode (radius, r>1 µm) aerosol particles, while values near 2 indicate mainly fine or

144   accumulation mode (r<1 µm) aerosol particles [*Holben et al.*, 1991; *Kaufman et al.*, 1992; *Eck et*

145   *al.*, 1999; *Reid et al.*, 1999; *Holben et al.*, 2001]. The absorption AOD or τ_{abs} is calculated for

146   each wavelength using equation (2):

$$\tau_{abs}(\lambda) = \tau_{ext}(\lambda) * [1-\omega_o(\lambda)] \tag{2}$$

147   [*Eck et al.*, 2010; *Russell et al.*, 2010; *Giles et al.*, 2011a]. Similar to α_{ext}, the spectral

148   dependence of τ_{abs} with λ on logarithmic scale gives the absorption Ångström exponent or α_{abs} in

149   equation (3):

$$\alpha_{abs} = -dln[\tau_{abs}(\lambda)]/dln(\lambda) \tag{3}$$

150 Assuming a spectrally constant index of refraction, very small spherical black carbon particles (r

151 ~0.01 μm) can have a λ^{-1} dependence or α_{abs} of 1.0 [*Bergstrom et al.*, 2002], while larger

152 optically effective black carbon particles (e.g., r>0.1 μm) may have α_{abs} values below 1.0 for

153 large cores and up to 1.6 for various shell coatings [*Lack and Cappa* 2010]. *Russell et al.* [2010]

154 analyzed AERONET pre-Version 1 almucantar retrievals from *Dubovik et al.* [2002] and showed

155 α_{abs} values vary between ~1.2 and 3.0 for Dust, ~0.75 and 1.3 for U/I, and ~1.2 and 2.0 for BB.

156 *Eck et al.* [2010] analyzed AERONET Version 2 almucantar retrievals and showed sites

157 dominated by optical mixtures of dust, smoke, and pollution had α_{abs} values between ~1.2 and

158 1.8 for mixed size particles (i.e., fine mode fraction of the AOD at 675 nm ranged between ~0.35

159 and 0.65). In the present study, the fine mode AOD (τ_f) and coarse mode AOD (τ_c) from the

160 almucantar retrieval—as inferred from the size distribution and refractive indices—were

161 interpolated to 550 nm using the linear fit of the logarithms of τ_f, τ (i.e., $\tau_f+\tau_c$) for 440, 675, and

162 870 nm wavelengths to calculate the fine mode fraction of the AOD [i.e., $\eta = \tau_f/(\tau_f+\tau_c)$] at 550

163 nm (η_{550nm}).

164   Nineteen AERONET sites were selected for the analysis based on the availability of an

165 extensive data record (i.e., greater than five data equivalent years of AOD measurements from

166 1999 to 2010) and the geographic distribution among aerosol source regions (Figure 1). The

167 sites were designated as one of four commonly used aerosol classifications: Dust, Mixed,

168 Urban/Industrial (U/I), and Biomass Burning (BB). The classifications were established based

169 on the source regions and known seasonal changes in aerosol type over these regions (see

170 references in Table 1). Further, these selected sites should be subject to high aerosol loading

171 (i.e., $\tau_{440nm}>0.4$) to meet the Version 2, Level 2.0 almucantar retrieval sensitivity requirement for

172 absorption parameters (e.g., ω_o, τ_{abs}) [*Dubovik et al.*, 2000; *Holben et al.*, 2006]. Sea salt (as well

173   as biogenic) aerosols as a dominant particle type category were not considered in this study since

174   τ_{500nm} is typically less than 0.1 for pure maritime environments [*Smirnov et al.*, 2002]; however,

175   for maritime locations affected by aerosol plumes (e.g., Saharan dust transport over Cape Verde

176   islands), τ_{440nm}>0.4 can be satisfied [*Smirnov et al.*, 2009]. Hence, the τ_{440nm}>0.4 criterion biases

177   the data set only to high aerosol loading periods to ensure enough radiometric sensitivity to

178   compute absorption reliably [*Dubovik et al.*, 2002]. Although Dust, U/I, and BB categories may

179   represent the dominant aerosol type, episodic aerosol incursions outside of their classification

180   category likely have occurred at any site during the analysis period (e.g., dust over Shirahama or

181   Lake_Argyle, biomass burning smoke over GSFC) [*Sano et al.*, 2003; *Qin and Mitchell* 2009;

182   *Eck et al.*, 2003b; *O'Neill et al.*, 2005]. The Mixed aerosol category encompasses sites primarily

183   affected by different mixtures of aerosol types (e.g., dust and pollution or dust and biomass

184   burning smoke mixtures) on a seasonal basis, increasing the probability of at least an optical

185   mixture state [*Derimian et al.*, 2006; *Eck et al.*, 2010]. Although no explicit seasonal

186   partitioning is performed, the τ_{440nm}>0.4 criterion captures mainly seasonal increases in aerosol

187   loading at some sites (e.g., GSFC and Mongu) [*Holben et al.*, 2001].

188   **3.0 Results**

189   **3.1   Retrieved Absorption Properties by Dominant Aerosol Type**

190   Dust particles aggregated with varying combinations of clay, quartz, and hematite exhibit

191   strong absorption in the blue wavelength region (e.g., 440 nm) with lower absorption in the

192   visible and near infrared wavelengths (i.e., ω_o increasing with wavelength) [*Sokolik and Toon*

193   1999]. For fine mode particles (r<1.0 μm in the volume size distribution), hygroscopic aerosol

194   particles (e.g., sulfates) have near neutral spectral dependence and high scattering efficiency

195   [*Dubovik et al.*, 2002]. Black carbon (BC) particles have the strongest absorption in the near-

196 infrared (ω_o decreasing with λ when the sole absorber), while aerosols composed of brown

197 carbon (BrC) or organic carbon (OC) exhibit stronger absorption in ultraviolet and visible bands

198 (ω_o increasing with λ when the sole absorber) [*Eck et al.*, 2009]. Varying concentrations of BC

199 particles optically mixed with dust, BrC, and/or OC can produce ambiguous ω_o wavelength

200 dependence (i.e., increasing, decreasing, or constant with λ); however, the net effect is stronger

201 absorption across the retrieved spectrum (e.g., 440 to 1020 nm) [*Dubovik et al.*, 2002; *Giles et*

202 *al.*, 2011a].

203   The AERONET Version 2, Level 2.0 absorption properties at each site are presented in

204 Figure 2 and Table 2 to provide an update to *Dubovik et al.* [2002] and *Russell et al.* [2010]. The

205 spectral ω_o behavior is similar to *Dubovik et al.* [2002] for most regions. For Solar Village

206 (Dust), Capo Verde (Dust), GSFC (U/I), Mexico City (U/I), and Mongu (BB), the ω_o differences

207 between *Dubovik et al.* [2002] and Table 2 (i.e., $\omega_{o\ Dubovik\ 2002} - \omega_{o\ Table\ 2}$) showed an overall

208 average decrease of 0.01 for these sites with the largest decrease of 0.02 spectrally for GSFC and

209 Capo Verde and smallest decrease ranging from 0 to 0.01 for Mongu. Notably, the ω_o standard

210 deviations are significantly greater by 0.01 to 0.03 in the present study than *Dubovik et al.* [2002]

211 for all five sites. Table 2 differs from *Dubovik et al.* [2002] due to utilizing different analysis

212 criteria (e.g., $\tau_{440nm}>0.4$ in Table 2 vs. $\tau_{1020nm}\geq0.3$ and $\alpha_{ext}\leq0.6$ for desert dust in *Dubovik et al.*

213 [2002]), implementing improved surface characterization and inversion quality checks in

214 Version 2 (as discussed in Section 2), and utilizing a larger data set (e.g., the number of ω_o

215 retrievals at GSFC is four times larger than *Dubovik et al.* [2002]). For ω_{o440nm} as a function of

216 τ_{440nm}, the R^2 values—calculated based on a second order fit—ranged from 0.0 to 0.16 for each

217 site, indicating weak correlation and only up to 16% of ω_{o440nm} variation was explained by τ_{440nm}.

218 Table 2 shows that the Dust category has the least variability among sites likely due to the

219   similar mineral composition, while the BB category has the largest variability likely due to

220   various fuel types and fuel combustion phases resulting from different relative BC emissions

221   [*Eck et al.*, 2003b]. The Mixed category ($0.33<\eta_{550nm}\leq0.66$) ω_o average shows strong spectral

222   absorption and dust-like ω_o spectra with stronger absorption at 440 nm due to significant dust

223   contribution to the optical mixture. *Sokolik and Toon* [1998] showed that varying hematite

224   amounts in dust can lead to increased absorption spectrally from the blue to near-infrared

225   wavelength region. Using $\alpha_{ext}<0.2$ to designate "pure dust" as suggested by *Kim et al.* [2011],

226   the overall "pure dust" average of ω_o for all Dust category sites is 0.91, 0.97, 0.97, 0.97 for the

227   440, 675, 870, and 1020 nm wavelengths, respectively. These "pure dust" ω_o values are lower

228   by up to 0.02, spectrally, than those reported by *Dubovik et al.* [2002] for Dust sites and are

229   lower by up to 0.01 for ω_o at 550 nm (logarithmically interpolated between 440 nm and 675 nm)

230   compared to similar sites analyzed by *Kim et al.* [2011]. Table 2 shows the Dust site averages

231   are lower than "pure dust," indicating possible incursions by other aerosols (e.g., biomass

232   burning smoke). *Eck et al.* [2010] and *Giles et al.* [2011a] also showed increasing absorption

233   with wavelength for decreasing α_{abs}, indicating an optical mixture and possibly aggregation of

234   dust and carbonaceous particles at Kanpur, India. We interpolated η to 550 nm using the linear

235   fit of the logarithms of τ_f, τ (i.e., $\tau_f + \tau_c$) and the 440, 675, and 870 nm wavelengths similar to *Lee*

236   *et al.* [2010]. In Figure 3a, the Mixed category for the coarse mode particles (η_{550nm}: 0.0-0.33)

237   resembles dust ω_o spectra as shown in Figure 2a. In Figure 3c, for fine mode particles (η_{550nm}:

238   0.66-1.0), the ω_o magnitudes and variability are similar to U/I or BB particle types categories but

239   with less ω_o spectral dependence possibly due to varying amounts of BC, BrC, and OC

240   [*Derimian et al.*, 2006; *Eck et al.*, 2009; 2010]. The average ω_o for α_{abs} binned between 1.5 and

241   2.0 shown by *Giles et al.* [2011a] at Kanpur closely resembles the absorption magnitude and

242 spectral shape of mixed aerosol types for the Mixed category ($0.33 < \eta_{550nm} \leq 0.66$) in Table 2 as

243 well as Figure 2b and Figure 3b suggesting various mixtures of aerosol particles contributing to

244 the absorption.

245   The ω_o and τ_{ext} are used to derive the τ_{abs} from AERONET data. τ_{abs} and α_{abs} were

246 averaged for each site based on dominant particle type category in Figure 4 and Table 2. For the

247 five sites (Solar Village, Capo Verde, GSFC, Mexico City, and Mongu), a comparison of

248 average α_{abs} values in Table 2 with *Russell et al.* [2010] for the 440-870 nm range shows the

249 largest difference in α_{abs} (i.e., $\alpha_{abs\,Russell\,2010} - \alpha_{abs\,Table\,2}$) at GSFC (-0.25) and Capo Verde (+1.2).

250 For the other three sites, the α_{abs} averages in Figure 4 are comparable to those reported by *Russell*

251 *et al.* [2010] and *Giles et al.* [2011a]. In Figure 5, the Mixed category was further stratified by

252 the η_{550nm} as in Figure 3. The coarse particle range (η_{550nm}: 0.0-0.33) shows similar α_{abs} (1.7-2.3)

253 as the Dust category (which is expected for dust dominated cases) and the fine particle range

254 (η_{550nm}: 0.66-1.0) shows an α_{abs} (0.8-1.5) similar to BB and U/I categories. The mixed size

255 particle range (η_{550nm}: 0.33-0.66) is nearly identical to the Mixed category α_{abs} (1.2-1.7) in

256 Figure 4b and similar to values reported by *Eck et al.* [2010]. As shown by *Bergstrom et al.*

257 [2007] and *Russell et al.* [2010], the α_{abs} may vary significantly when considering the aerosol

258 particle size between fine and coarse modes; however, when considering U/I and BB aerosols

259 within the fine particle range, significant overlap results in α_{abs}. The sensitivity of α_{abs} with

260 respect to input parameters will be investigated in the next section.

261 **3.2   Absorption Ångström Exponent Sensitivity Study**

262   The retrieved values of α_{abs} have a normal distribution (Figure 6) when calculating α_{abs}

263 using three wavelengths (440-675-870 nm) for each dominant aerosol type. *Russell et al.* [2010]

264 showed that the average α_{abs} values generally decreased with increasing spectral range possibly

265 due in part to the crude surface reflectance assumption made in early AERONET analysis (as

266 discussed in Section 3.1), while *Gyawali et al.* [2012] showed an increasing α_{abs} values with

267 increasing spectral range for clean and polluted days during winter in Reno, Nevada. However,

268 increasing or decreasing trends of α_{abs} depend on the wavelength interval [*Lack and Cappa*

269 2010]. These α_{abs} values computed from 440-675-870 nm wavelength range have large

270 variability with standard deviations ranging from ±0.3 to ±0.6 (1.76±0.58 for Dust; 1.53±0.44 for

271 Mixed; 1.21±0.37 for U/I; 1.35±0.35 for BB). Individual α_{abs} retrieval calculations [α_{abs} (Dust):

272 ~0-4; α_{abs} (Mixed): ~0-3.5; α_{abs} (U/I): ~0-2; α_{abs} (BB): ~0-2.5] are within the range of all

273 dominant particle types; therefore, α_{abs} should not be used alone to determine aerosol types

274 without the use of other information (e.g., aerosol size). Further, Figure 6 shows a significant

275 percentage of α_{abs} below 1.0, which is the black carbon limit for very small particles [*Bergstrom*

276 *et al.*, 2002]. However, *Lack and Cappa* [2010] suggested α_{abs} (from 380-750 nm) values for

277 larger optically effective BC particles may exist between ~-0.2 and 1.6 depending on the BC

278 coating material. Nonetheless, the U/I category has over 22% of the α_{abs} retrievals below 1.0,

279 while the other categories have ~10% of the data below α_{abs} of 1.0 also possibly due to the

280 uncertainty of the retrieved ω_o.

281   A sensitivity study of α_{abs} was performed to test the response of α_{abs} by varying ω_o for

282 each wavelength (i.e., 440, 675, and 870 nm) and holding τ_{ext} constant (i.e., AOD cannot be

283 perturbed since it is used in the calculation of ω_o retrieval). First, ω_o was varied by ±0.03, the

284 current AERONET ω_o uncertainty estimate [*Dubovik et al.*, 2002]. Additional tests included

285 varying ω_o by ±0.01, ±0.02, and ±0.04 to show the variability of α_{abs} with various degrees of ω_o

286 uncertainty. Different spectral ω_o inputs schemes were implemented to determine the α_{abs}

287 response by varying ω_o equally across all wavelengths, by perturbing ω_o at only one end point in

288   the 440-675-870 nm wavelength set (i.e., 440 nm or 870 nm), and by perturbing ω_o at 440 nm or

289   870 nm in the 440-870 nm wavelength pair (i.e., excluding 675 nm). Positive ω_o perturbation

290   may approach values of 1.0 (i.e., absolute scattering) and can produce large positive or negative

291   α_{abs} due to very low τ_{abs}. To prevent such cases, the ω_o magnitude was limited to less than 0.995

292   for positive ω_o perturbations for all wavelengths resulting in a reduced data subset.

293   Table 3 shows the sensitivity of α_{abs} to perturbations in ω_o. The perturbation of ±0.03 ω_o

294   (the current estimated uncertainty) changed α_{abs} by at least ~±0.6 for Dust, ~±0.2 for Mixed, and

295   ~±0.1 for U/I and BB. The perturbations of ω_o by ±0.02 showed ~0.1 smaller corresponding

296   change in α_{abs} with respect to ±0.03 ω_o perturbations for Dust and less than 0.05-0.10 for the

297   other categories. Perturbations of ω_o by ±0.04 showed large deviations from the unperturbed

298   data set, indicating much greater uncertainty for α_{abs} with increasing ω_o uncertainty. The

299   simulated overestimation of spectral ω_o for U/I and BB (i.e., $\delta\omega_o$=-0.03) showed a higher $\delta\alpha_{abs}$

300   suggesting a possibility that the unperturbed α_{abs} is underestimated and may possibly, at least

301   partly, explain α_{abs} below 1.0 in these categories. However, *Lack and Cappa* [2010] determined

302   that the large α_{abs} variation (-0.2 and 1.3 for the 380-750 nm wavelength range) for BC particles

303   with coatings are possible and α_{abs} values less than 1.0 may occur with larger BC particles (e.g.,

304   r_{core}>0.1 μm and r_{shell}>0.25 μm). *Gyawali et al.* [2012] showed laboratory measurements of

305   kerosene soot particles have α_{abs} values of ~0.8 for the 355-1020 nm range and in situ

306   measurement values of α_{abs} measured during the Reno, Nevada, winter period varied for clean

307   days (PM$_{2.5}$<40 μg/m^3) between ~1.0 and 1.4 and for polluted days (PM$_{2.5}$≥40 μg/m^3) between

308   0.9 and 1.2 for the 405-870 nm wavelength range. Although these model simulations and

309   laboratory and in situ measurements suggest α_{abs} values may occur below 1.0, AERONET

310   remotely sensed values of α_{abs} have not yet been compared to coincident column-effective in situ

311   measurements (e.g., measured by aircraft) but this analysis will be addressed in future work. In

312   the present analysis, the simulated underestimation of spectral ω_o (i.e., $\delta\omega_o$=+0.03) for Dust and

313   Mixed indicates possible underestimation of the unperturbed α_{abs}, which could also result in α_{abs}

314   below 1.0. Table 3 also shows the Dust and Mixed categories change in the same direction as

315   the ω_o perturbation possibly due to weak spectral dependence of τ_{ext}, while U/I and BB

316   categories have the opposite response. Two additional tests were conducted by perturbing ω_o

317   using the wavelength pair (440-870 nm) and only varying the end points of the 440-675-870 nm

318   set and the differences between unperturbed α_{abs} averages were minimal (not shown). However,

319   perturbing one ω_o end point for either the 440-870 nm wavelength pair (not shown) or the 440-

320   675-870 nm set (Table 3) produced very large deviations in α_{abs} by up to ~1.2 for Dust, ~0.7 for

321   Mixed, ~1.0 for U/I, and ~0.6 for BB. The perturbation of end points simulates atypical behavior

322   of the instrument while deployed in the field (e.g., anomalous filter degradation) showing

323   potential issues in using real-time data products unless further screening is implemented, such as

324   the instrument collimator consistency checks (stated in Section 2.0), which may be utilized to

325   help remove ω_o artifacts (i.e., collimator or sensor head window obstructions) and improve the

326   reliability of α_{abs} retrievals. These sensitivity tests quantified the effect of the reduction of ω_o

327   uncertainty on improving estimates of α_{abs}.

328   **3.3   Cluster Analysis by Dominant Aerosol Type**

329   Knowledge of aerosol particle spectral absorption provides insight to determine aerosol

330   particle dominance of dust, carbonaceous matter, or hygroscopic aerosols (e.g., sulfates, nitrates,

331   or sea salt). While the co-albedo (or 1-ω_o) indicates the magnitude of absorption and α_{abs}

332   provides some indication of the dominance of carbonaceous particles (e.g., BC, BrC, and OC) or

333   iron oxides in dust, these parameters alone cannot fully describe the aerosol particle type.

15

334 Recent studies have suggested applying an aerosol particle size parameter (e.g., α_{ext} or η) to

335 separate larger dust particles from other aerosol types and mixtures [*Lee et al.*, 2010; *Russell et*

336 *al.*, 2010; *Giles et al.*, 2010; 2011a; 2011b]. In this section, several years of AERONET

337 retrievals of ω_{o440nm}, $\alpha_{abs440-870nm}$, $\alpha_{ext440-870nm}$, and η_{550nm} (with wavelength subscripts removed

338 hereafter) were analyzed for each dominant aerosol type category using a density based

339 clustering utilizing the Voronoi tessellation [*Voronoi* 1908; *Ishimoto et al.*, 2010] to determine

340 the relative concentration of points (density = 1/polygon area) for each absorption and size

341 relationship. In these density plots (e.g., Figures 7-10), the high density represents the primary

342 mode for the dominant aerosol particle type category. Various clustering techniques were

343 attempted previously to categorize dominant aerosol particle type at AERONET sites [*Cattrall et*

344 *al.*, 2005; *Omar et al.*, 2005; *Levy et al.*, 2007; *Qin and Mitchell* 2009; *Russell et al.*, 2010,

345 *Boselli et al.*, 2012]. For each absorption and size relationship and aerosol type category in this

346 study (Figure 11), dominant aerosol particle clusters were computed using averages weighted by

347 density magnitudes normalized to a 64-level scale (corresponding to a 64-bit color scale).

348 Although weighting reduces the bias introduced by outliers affecting the normal average,

349 additional thresholds were applied to the aerosol size parameters. To further define weighted

350 cluster averages, the α_{ext} cluster averages utilized a 0.8 threshold, where >0.8 indicates mainly

351 small sub-micron radius particles and ≤0.8 is mainly large super-micron radius particles (where

352 $\alpha_{ext440-870nm}$=0.8 is approximately equivalent to η_{500nm}=0.5 as shown for example by *Eck et al.*

353 [2005; 2010]). In addition, the η cluster averages were defined using thresholds of 0.0 to ≤0.33

354 (for coarse mode dominated particles), 0.33 to ≤0.66 (for mixed size), and >0.66 (for fine mode

355 dominated particles). For the BB category (Figure 11c and Figure 11d), cluster separation was

356   imposed to calculate two additional clusters using a ω_{o440nm} threshold of 0.90 based on the

357   density cluster analyses shown in Figure 9 and Figure 10.

358   The relationships of aerosol absorption and size are analyzed with respect to the

359   dominant aerosol type category. For Figures 7-10, the primary density clusters are clear

360   (denoted by orange and red regions representing relative value levels of ~45 to 64). For

361   example, the Dust category shows a cluster in the region with α_{ext} of ~0.2-0.3 and η of ~0.2-0.3,

362   indicative of domination by coarse mode particles. To provide a better assessment of the

363   clusters, the weighted cluster average and one standard deviation was calculated for each

364   parameter shown in Figure 11. In Figure 11a and Figure 11b, the primary Dust clusters show

365   variation of the α_{abs} mainly between 1.5 and 2.3, which are slightly lower values than reported by

366   *Russell et al.* [2010]. In Figure 11c and Figure 11d, ω_o also varies significantly in the primary

367   Dust cluster from 0.89-0.93, possibly due to variation in mineral composition of dust [*Sokolik*

368   *and Toon* 1999]. For α_{ext} (Figure 11a and Figure 11c), the Mixed aerosol type category has two

369   primary density clusters (1) "Mixed-Large Particle" cluster for mainly super-micron particles

370   (centered at α_{ext}~0.4) and (2) "Mixed-Small Particle" for mainly submicron particles (centered at

371   α_{ext}~1.25). In comparison to the Dust cluster, the Mixed-Large Particle cluster tends to have a

372   slightly smaller contribution to larger particles in the 0.3-0.6 α_{ext} range, while η relationships

373   (Figure 11b and Figure 11d) show the Mixed-Large Particle cluster for coarse particles is nearly

374   identical to the Dust cluster. The Mixed category for mixed sizes ($0.33 < \eta_{550nm} \leq 0.66$) does not

375   show high cluster density due to varying sizes and contributions of the aerosol particles

376   containing dust with pollution or biomass burning smoke with strongly varying absorption [*Eck*

377   *et al.*, 2010]. In Figure 11, the Mixed-Small Particle clusters (α_{ext}~1.0 to 1.5; also η~0.8-0.95)

378   show significant variability likely due to variation in carbonaceous particle contribution

379   (primarily BC but also OC) with α_{abs} between ~1.3 and 1.7 similar to those observed in Kanpur

380   for fine mode dominated cases by *Giles et al.* [2011a]. As indicated by *Russell et al.* [2010] and

381   shown in Figure 6, the U/I and BB category types for the α_{abs} and α_{ext} relationship tend to overlap

382   each other. For primary density clusters in these two categories, the α_{abs} vary from ~1.1 to 1.8.

383   Until the ω_o uncertainty is known and constrained further (given the sensitivity results of Section

384   3.2), the usefulness of α_{abs} to determine various carbonaceous aerosol particles is doubtful except

385   in separating cases dominated by BC from cases dominated by BrC or OC. A "region" of higher

386   α_{abs} values from the density cluster analysis for BB (Figure 7d and Figure 8d) likely indicates

387   aged smoke from primarily smoldering combustion containing higher concentrations of BrC or

388   OC and relatively low BC [*Eck et al.*, 2009; *Moosmüller et al.*, 2009; 2011], especially above an

389   α_{abs} of 1.6 for fine mode particles [*Lack and Cappa* 2010] and also supported by Figure 9d and

390   Figure 10d with ω_o above 0.90. For example, according to *Eck et al.* [2009] and *Arola et al.*

391   [2011], significant absorbing OC concentrations and high OC/BC ratios likely occurred at the

392   Bonanza Creek site where Table 2 shows the spectral ω_o average is ~0.95 and averages of α_{abs},

393   α_{ext}, and η_{550nm} are 1.8, 1.5, and 0.96, respectively. However, the ω_o relationships (Figure 11c

394   and Figure 11d) show more cluster separation than α_{abs} relationships (Figure 11a and Figure

395   11b). In Figure 11d, the primary U/I cluster is centered above 0.95, while the main BB cluster is

396   centered on ~0.89 with two BB sub-clusters centered on ~0.93 and ~0.87 ω_o (calculated by using

397   ω_o threshold of 0.90); however, the BB clusters overlap with the Mixed-Small Particle cluster.

398   The ω_{o440nm} and $\alpha_{ext440-870\ nm}$ relationship (Figure 11c) shows distinct high density clusters in all

399   categories (i.e., between Dust and Mixed-Large Particle, and among Mixed-Small Particle-U/I-

400   BB, and between U/I-BB clusters), while minimal overlap occurs with the U/I and the less

401   absorbing ($\omega_o > 0.90$) BB sub-cluster. Nonetheless, the analysis has shown that the ω_{o440nm} and

402    $\alpha_{ext440-870 \, nm}$ relationship demonstrates that the dominant particle type may be ascertained simply

403   from commonly measured or retrieved absorption and size parameters.

404   **4.0 Conclusions**

405   In this paper, absorption properties (i.e., single scattering albedo and absorption

406   Ångström exponent) were averaged for 19 AERONET sites to show correspondence to

407   representative aerosol source regions. Sensitivity tests on absorption Ångström exponent were

408   performed by varying the single scattering albedo within plausible constraints based on

409   uncertainty estimates. Lastly, the absorption and size relationships were evaluated and compared

410   to each other based on the dominant aerosol type categorizations.

411   (1) A summary of aerosol absorption parameters from the AERONET Version 2, Level

412   2.0 almucantar retrievals was presented to expand upon previous work using pre-Version 1

413   retrievals. A comparison of five sites common to *Dubovik et al.* [2002] showed a 0.01 average

414   spectral (from 440 to 1020 nm) decrease in single scattering albedo (ω_o) with the largest

415   decreases spectrally of 0.02 at Capo Verde and GSFC AERONET sites. The average absorption

416   Ångström exponent ($\alpha_{abs440-870 \, nm}$) computed from Version 2 retrievals was 1.2 lower for Capo

417   Verde and 0.25 higher for GSFC than reported by *Russell et al.* [2010] computed from pre-

418   Version 1 retrievals. Aerosol mixtures exhibited stronger spectral absorption (i.e., lower ω_o) and

419   increased dominance of absorbing carbonaceous particles (i.e., lower $\alpha_{abs440-870 \, nm}$) than for dust

420   alone, possibly due to an optical mixture state (e.g., dust and smoke or dust and pollution) or the

421   aggregation of dust and carbonaceous particles.

422   (2) The $\alpha_{abs440-870 \, nm}$ calculated from AERONET data ranged from ~0 to 3.5 among

423   dominant aerosol type categories. Frequency distributions of $\alpha_{abs440-870 \, nm}$ exhibited significant

424   overlap among aerosol types, while the Urban/Industrial and Biomass Burning distributions were

425   nearly identical for $\alpha_{abs440-870\,nm}$ values above 1.0. Further, frequency distributions showed

426   approximately 10% of the α_{abs} retrievals had values below 1.0 for most aerosol categories but as

427   high as 22% for the Urban/Industrial category.

428   (3) A sensitivity study perturbing the ω_o by the current AERONET uncertainty (±0.03)

429   showed α_{abs} changes by at least ~±0.6 for Dust, ~±0.2 for Mixed, and ~±0.1 for Urban/Industrial

430   and Biomass Burning. The sensitivity study quantified the improvement in estimates of α_{abs}

431   resulting from reducing the ω_o uncertainty. Variations within the uncertainty of ω_o retrievals

432   may explain some of the observed α_{abs} values below 1.0 in AERONET data although in situ

433   measurements suggest that some of these α_{abs} values may be real depending on the aerosol

434   particle composition and size.

435   (4) Absorption and size relationships were examined using density cluster analysis for

436   each dominant aerosol particle type. The ω_{o440nm} vs. $\alpha_{ext440-870\,nm}$ relationship showed at least five

437   distinct aerosol type clusters [Dust, Mixed-Large Particle, Mixed-Small Particle,

438   Urban/Industrial, and Biomass Burning (with two sub-clusters)], while the $\alpha_{abs440-870\,nm}$ vs. $\alpha_{ext440-}$

439    $_{870\,nm}$ relationship had fewer distinct clusters due to less definition for mainly small aerosol

440   particles ($\alpha_{ext440-870\,nm} > 1.5$).

441   We showed the ω_{o440nm} and $\alpha_{ext440-870nm}$ relationship provided a better clustering

442   relationship and it may be applied to measurements of aerosol absorption and size properties

443   derived from surface- and potentially future space-based platforms. From ω_{o440nm} and $\alpha_{ext440-870}$

444    $_{nm}$ clusters, at least, major dominant aerosols types and some mixtures can be identified using

445   common aerosol absorption and size parameters without prior knowledge of aerosol transport or

446 source regions. Alternatively, when ω_o is not available but $\alpha_{abs440-870nm}$ is (e.g., using spectral

447 absorption coefficients measured in situ to calculate α_{abs}), $\alpha_{abs440-870nm}$ vs. $\alpha_{ext440-870nm}$ may also

448 provide a reasonable aerosol type classification. A combination of ω_{o440nm} vs. $\alpha_{ext440-870nm}$ and

449 $\alpha_{abs440-870nm}$ vs. $\alpha_{ext440-870nm}$ relationships could provide a more detailed classification of aerosol

450 composition which will require further investigation.

5.0 Acknowledgements

References

Ångström, A. (1964), The parameters of atmospheric turbidity, *Tellus*, *16*(1), 64–75.

Arola, A., Schuster, G., Myhre, G., Kazadzis, S., Dey, S., and Tripathi, S. N. (2011), Inferring absorbing organic carbon content from AERONET data, Atmos. Chem. Phys., 11, 215-225, doi:10.5194/acp-11-215-2011.

Basart, S., Pérez, C., Cuevas, E., Baldasano, J. M., and Gobbi, G. P. (2009), Aerosol characterization in Northern Africa, Northeastern Atlantic, Mediterranean Basin and Middle East from direct-sun AERONET observations, *Atmos. Chem. Phys.*, *9*, 8265-8282, doi:10.5194/acp-9-8265-2009.

Bergstrom, R. W., P. B. Russell, and P. Hignett (2002), Wavelength dependence of the absorption of black carbon particles: Predictions and results from the TARFOX experiment and implications for the aerosol single scattering albedo, *J. Atmos. Sci.*, *59*, 567–577, doi:10.1175/1520-0469(2002) 059<0567:WDOTAO>2.0.CO;2.

Bergstrom, R. W., P. Pilewskie, P. B. Russell, J. Redemann, T. C. Bond, P. K. Quinn, and B. Sierau (2007), Spectral absorption properties of atmospheric aerosols, *Atmos. Chem. Phys.*, *7*, 5937–5943, doi:10.5194/acp-7-5937-2007.

Boselli A., R. Caggiano, C. Cornacchia, F. Madonna, L. Mona, M. Macchiato, G. Pappalardo, and S. Trippetta (2012), Multi year sun-photometer measurements for aerosol characterization in a Central Mediterranean site, *J. Atmos. Res.*, *104-105*, 98-110, doi: 10.1016/j.atmosres.2011.08.002.

Burton, S. P., Ferrare, R. A., Hostetler, C. A., Hair, J. W., Rogers, R. R., Obland, M. D., Butler, C. F., Cook, A. L., Harper, D. B., and Froyd, K. D. (2012), Aerosol classification using airborne High Spectral Resolution Lidar measurements – methodology and examples, Atmos. Meas. Tech., 5, 73-98, doi:10.5194/amt-5-73-2012.

Cattrall, C., J. Reagan, K. Thome, and O. Dubovik (2005), Variability of aerosol and spectral lidar and backscatter and extinction ratios of key aerosol types derived from selected Aerosol Robotic Network locations, *J. Geophys. Res.*, *110*, D10S11, doi:10.1029/2004JD005124.

Derimian, Y., A. Karnieli, Y. J. Kaufman, M. O. Andreae, T. W. Andreae, O. Dubovik, W. Maenhaut, I. Koren, and B. N. Holben (2006), Dust and pollution aerosols over the Negev desert, Israel: Properties, transport, and radiative effect, *J. Geophys. Res.*, *111*, D05205, doi:10.1029/2005JD006549.

Derimian, Y., A. Karnieli, Y. J. Kaufman, M. O. Andreae, T. W. Andreae, O. Dubovik, W. Maenhaut, and I. Koren (2008), The role of iron and black carbon in aerosol light absorption, *Atmos. Chem. Phys.*, *8*, 3623–3637, doi:10.5194/acp-8-3623-2008.

497 Dey, S., S. N. Tripathi, R. P. Singh, and B. N. Holben (2004), Influence of dust storms on the
498   aerosol optical properties over the Indo-Gangetic basin, *J. Geophys. Res.*, *109*, D20211,
499   doi:10.1029/2004JD004924.

500 Diner, D. J., G. P. Asner, R. Davies, Y. Knyazikhin, J.-P. Muller, A. W. Nolin, B. Pinty, C. B.
501   Schaaf, and J. Stroeve (1999), New Directions in Earth Observing: Scientific
502   Applications of Multiangle Remote Sensing, *Bull. Amer. Meteor. Soc.*, *80*, 2209–2228,
503   doi: http://dx.doi.org/10.1175/1520-0477(1999)080<2209:NDIEOS>2.0.CO;2.

504 Dubovik, O., and M. D. King (2000), A flexible inversion algorithm for retrieval of aerosol
505   optical properties from Sun and sky radiance measurements, *J. Geophys. Res.*, *105*,
506   20,673–20,696, doi:10.1029/2000JD900282.

507 Dubovik, O., A. Smirnov, B. N. Holben, M. D. King, Y. J. Kaufman, T. F. Eck, and I. Slutsker
508   (2000), Accuracy assessments of aerosol optical properties retrieved from AERONET
509   Sun and sky-radiance measurements, *J. Geophys. Res.*, *105*, 9791–9806,
510   doi:10.1029/2000JD900040.

511 Dubovik, O., B. N. Holben, T. F. Eck, A. Smirnov, Y. J. Kaufman, M. D. King, D. Tanre, and I.
512   Slutsker (2002), Variability of absorption and optical properties of key aerosol types
513   observed in worldwide locations, *J. Atmos. Sci.*, *59*, 590–608, doi:10.1175/1520-
514   0469(2002)059<0590:VOAAOP>2.0.CO;2.

515 Dubovik, O., et al. (2006), Application of spheroid models to account for aerosol particle
516   nonsphericity in remote sensing of desert dust, *J. Geophys. Res.*, *111*, D11208,
517   doi:10.1029/2005JD006619.

518 Eck, T. F., B. N. Holben, J. S. Reid, O. Dubovik, A. Smirnov, N. T. O'Neill, I. Slutsker, and S.
519   Kinne (1999), Wavelength dependence of the optical depth of biomass burning, urban,
520   and desert dust aerosols, *J. Geophys. Res.*, *104*(D24), 31,333–31,349,
521   doi:10.1029/1999JD900923.

522 Eck, T. F., et al. (2003a), Variability of biomass burning aerosol optical characteristics in
523   southern Africa during the SAFARI 2000 dry season campaign and a comparison of
524   single scattering albedo estimates from radiometric measurements, *J. Geophys.
525   Res.*,*108*(D13), 8477, doi:10.1029/2002JD002321.

526 Eck, T. F., B. N. Holben, J. S. Reid, N. T. O'Neill, J. S. Schafer, O. Dubovik, A. Smirnov, M. A.
527   Yamasoe, and P. Artaxo (2003b), High aerosol optical depth biomass burning events: A
528   comparison of optical properties for different source regions, *Geophys. Res. Lett.*, *30*(20),
529   2035, doi:10.1029/2003GL017861.

530 Eck, T. F., et al. (2005), Columnar aerosol optical properties at AERONET sites in central
531   eastern Asia and aerosol transport to the tropical mid-Pacific, *J. Geophys. Res.*, *110*,
532   D06202, doi:10.1029/2004JD005274.

533 Eck, T. F., et al. (2008), Spatial and temporal variability of column-integrated aerosol optical
534   properties in the southern Arabian Gulf and United Arab Emirates in summer, *J.
535   Geophys. Res.*, *113*, D01204, doi:10.1029/2007JD008944.

536 Eck, T. F., et al. (2009), Optical properties of boreal region biomass burning aerosols in central
537   Alaska and seasonal variation of aerosol optical depth at an Arctic coastal site, *J.*
538   *Geophys. Res.*, *114*, D11201, doi:10.1029/2008JD010870.

539 Eck, T. F., et al. (2010), Climatological aspects of the optical properties of fine/coarse mode
540   aerosol mixtures, *J. Geophys. Res.*, *115*, D19205, doi:10.1029/2010JD014002.

541 Giles, D. M., B. Hoblen, T. F. Eck, A. Sinyuk, R.R. Dickerson, A. M. Thompson, I. Slutsker, Z.
542   Li, S. N. Tripathi, R. Singh, and G. Zibordi (2010), Identifying Aerosol Type/Mixture
543   from Aerosol Absorption Properties Using AERONET, *Eos Trans. AGU*, *91*(26), West.
544   Pac. Geophys. Meet. Suppl., Abstract A33D-05.

545 Giles, D. M., et al. (2011a), Aerosol properties over the Indo-Gangetic Plain: A mesoscale
546   perspective from the TIGERZ experiment, *J. Geophys. Res.*, *116*, D18203,
547   doi:10.1029/2011JD015809.

548 Giles, D. M., B. N. Holben, T. F. Eck, A. Sinyuk, A. Smirnov, I. Slutsker, R. R. Dickerson, A.
549   M. Thompson, and J. S. Schafer (2011b), Dominant Aerosol Particle Type/Mixture
550   Identification at Worldwide Locations Using the Aerosol Robotic Network (AERONET),
551   Abstract A14E-07 presented at 2011 Fall Meeting, AGU, San Francisco, Calif., 5-9 Dec.

552 Gobbi, G. P., Kaufman, Y. J., Koren, I., and Eck, T. F. (2007), Classification of aerosol
553   properties derived from AERONET direct sun data, *Atmos. Chem. Phys.*, *7*, 453-458,
554   doi:10.5194/acp-7-453-2007.

555 Gyawali, M., et al. (2012), Photoacoustic optical properties at UV, VIS, and near IR wavelengths
556   for laboratory generated and winter time ambient urban aerosols, *Atmos. Chem. Phys.*, *12*,
557   2587-2601, doi:10.5194/acp-12-2587-2012.

558 Holben, B. N., T. F. Eck, and R. S. Fraser (1991), Temporal and spatial variability of aerosol
559   optical depth in the Sahel region in relation to vegetation remote sensing, *Int. J. Remote*
560   *Sens.*, *12*(6), 1147–1163, doi:10.1080/01431169108929719.

561 Holben, B. N., et al. (1998), AERONET−A federated instrument network and data archive for
562   aerosol characterization, *Remote Sens. Environ.*, *66*, 1–16, doi:10.1016/S0034-
563   4257(98)00031-5.

564 Holben, B. N., et al. (2001), An emerging ground-based aerosol climatology: Aerosol optical
565   depth from AERONET, *J. Geophys. Res.*, *106*(D11), 12,067–12,097,
566   doi:10.1029/2001JD900014.

567 Holben, B. N., T. F. Eck, I. Slutsker, A. Smirnov, A. Sinyuk, J. Schafer, D. Giles, and O.
568   Dubovik (2006), AERONET's Version 2.0 quality assurance criteria, in Remote Sensing
569   of the Atmosphere and Clouds, edited by S.-C. Tsay et al., *Proc. SPIE*, *6408*, 64080Q,
570   doi:10.1117/12.706524.

571 Ishimoto, H., Y. Zaizen, A. Uchiyama, K. Masuda, Y. Mano (2010), Shape modeling of mineral
572   dust particles for light-scattering calculations using the spatial Poisson−Voronoi
573   tessellation, *J. of Quant. Spect. and Rad. Trans.*, *111*, 16, doi:10.1016/j.jqsrt.2010.06.018.

574 Jeong, M.-J., and Z. Li (2005), Quality, compatibility, and synergy analyses of global aerosol
575   products derived from the advanced very high resolution radiometer and Total Ozone
576   Mapping Spectrometer, *J. Geophys. Res.*, *110*, D10S08, doi:10.1029/2004JD004647.

577 Johnson, B. T., S. Christopher, J. M. Haywood, S. R. Osborne, S. McFarlane, C. Hsu, C.
578   Salustro, and R. Kahn (2009), Measurements of aerosol properties from aircraft and
579   ground-based remote sensing: A case-study from the Dust and Biomass-burning
580   Experiment (DABEX), *Q. J. R. Met. Soc.*, *135*, doi:10.1002/qj.420.

581 Kahn, R. A., B. J. Gaitley, M. J. Garay, D. J. Diner, T. F. Eck, A. Smirnov, and B. N. Holben
582   (2010), Multiangle Imaging SpectroRadiometer global aerosol product assessment by
583   comparison with the Aerosol Robotic Network, *J. Geophys. Res.*, *115*, D23209,
584   doi:10.1029/2010JD014601.

585 Kalapureddy, M. C. R., D. G. Kaskaoutis, P. Ernest Raj, P. C. S. Devara, H. D. Kambezidis, P.
586   G. Kosmopoulos, and P. T. Nastos (2009), Identification of aerosol type over the Arabian
587   Sea in the premonsoon season during the Integrated Campaign for Aerosols, Gases and
588   Radiation Budget (ICARB), *J. Geophys. Res.*, *114*, D17203, doi:10.1029/2009JD011826.

589 Kaufman, Y. J., A. Setzer, D. Ward, D. Tanre, B. N. Holben, P. Menzel, M. C. Pereira, and R.
590   Rasmussen (1992), Biomass Burning Airborne and Spaceborne Experiment in the
591   Amazonas (BASE-A), *J. Geophys. Res.*, *97*(D13), 14,581–14,599,
592   doi:10.1029/92JD00275.

593 Kim, D., Chin, M., Yu, H., Eck, T. F., Sinyuk, A., Smirnov, A., and Holben, B. N. (2011), Dust
594   optical properties over North Africa and Arabian Peninsula derived from the AERONET
595   dataset, *Atmos. Chem. Phys.*, *11*, 10733-10741, doi:10.5194/acp-11-10733-2011.

596 Lack, D. A. and Cappa, C. D. (2010), Impact of brown and clear carbon on light absorption
597   enhancement, single scatter albedo and absorption wavelength dependence of black
598   carbon, *Atmos. Chem. Phys.*, *10*, 4207-4220, doi:10.5194/acp-10-4207-2010.

599 Leahy, L. V., T. L. Anderson, T. F. Eck, and R. W. Bergstrom (2007), A synthesis of single
600   scattering albedo of biomass burning aerosol over southern Africa during SAFARI 2000,
601   *Geophys. Res. Lett.*, *34*, L12814, doi:10.1029/2007GL029697.

602 Lee J., J. Kim, C.H. Song, S.B. Kim, Y. Chun, B.J. Sohn, and B.N. Holben (2010),
603   Characteristics of aerosol types from AERONET sunphotometer measurements, *Atmos.*
604   *Environ.*, *44*, 26, doi: 10.1016/j.atmosenv.2010.05.035.

605 Levy, R. C., L. A. Remer, and O. Dubovik (2007), Global aerosol optical properties and
606   application to Moderate Resolution Imaging Spectroradiometer aerosol retrieval over
607   land, *J. Geophys. Res.*, *112*, D13210, doi:10.1029/2006JD007815.

608 Mélin, F., and G. Zibordi (2005), Aerosol variability in the Po Valley analyzed from automated
609   optical measurements, *Geophys. Res. Lett.*, *32*, L03810, doi:10.1029/2004GL021787.

610 Mielonen, T., A. Arola, M. Komppula, J. Kukkonen, J. Koskinen, G. de Leeuw, and K. E. J.
611   Lehtinen (2009), Comparison of CALIOP level 2 aerosol subtypes to aerosol types

derived from AERONET inversion data, *Geophys. Res. Lett.*, *36*, L18804, doi:10.1029/2009GL039609.

Mitchell, R. M., D. M. O'Brien, and S. K. Campbell (2006), Characteristics and radiative impact of the aerosol generated by the Canberra firestorm of January 2003, *J. Geophys. Res.*, *111*, D02204, doi:10.1029/2005JD006304.

Moosmüller H., R. K. Chakrabarty, W. P. Arnott (2009), Aerosol light absorption and its measurement: A review, *J. of Quant. Spect. and Rad. Trans.*, *110*, 11, doi:10.1016/j.jqsrt.2009.02.035.

Moosmüller, H., Chakrabarty, R. K., Ehlers, K. M., and Arnott, W. P. (2011), Absorption Ångström coefficient, brown carbon, and aerosols: basic concepts, bulk matter, and spherical particles, *Atmos. Chem. Phys.*, *11*, 1217-1225, doi:10.5194/acp-11-1217-2011.

Müller, D., et al. (2010), Mineral dust observed with AERONET Sun photometer, Raman lidar, and in situ instruments during SAMUM 2006: Shape-independent particle properties, *J. Geophys. Res.*, *115*, D07202, doi:10.1029/2009JD012520.

Omar, A. H., J.-G. Won, D. M. Winker, S.-C. Yoon, O. Dubovik, and M. P. McCormick (2005), Development of global aerosol models using cluster analysis of Aerosol Robotic Network (AERONET) measurements, *J. Geophys. Res.*, *110*, D10S14, doi:10.1029/2004JD004874.

O'Neill, N. T., S. Thulasiraman, T. F. Eck, and J. S. Reid (2005), Robust optical features of fine mode size distributions: Application to the Québec smoke event of 2002, *J. Geophys. Res.*, *110*, D11207, doi:10.1029/2004JD005157.

Prasad, A. K., and R. P. Singh (2007), Changes in aerosol parameters during major dust storm events (2001–2005) over the Indo-Gangetic Plains using AERONET and MODIS data, *J. Geophys. Res.*, *112*, D09208, doi:10.1029/2006JD007778.

Qin, Y. and Mitchell, R. M. (2009), Characterisation of episodic aerosol types over the Australian continent, *Atmos. Chem. Phys.*, *9*, 1943-1956, doi:10.5194/acp-9-1943-2009.

Reid, J. S., T. F. Eck, S. A. Christopher, P. V. Hobbs, and B. Holben (1999), Use of the Ångstrom exponent to estimate the variability of optical and physical properties of aging smoke particles in Brazil, *J. Geophys. Res.*, *104*(D22), 27,473–27,489, doi:10.1029/1999JD900833.

Reid, J. S., et al (2003)., Analysis of measurements of Saharan dust by airborne and ground-based remote sensing methods during the Puerto Rico Dust Experiment (PRIDE), *J. Geophys. Res.*, *108*(D19), 8586, doi:10.1029/2002JD002493.

Russell, P. B., R. W. Bergstrom, Y. Shinozuka, A. D. Clarke, P. F. DeCarlo, J. L. Jimenez, J. M. Livingston, J. Redemann, O. Dubovik, and A. Strawa (2010), Absorption Ångstrom Exponent in AERONET and related data as an indicator of aerosol composition, *Atmos. Chem. Phys.*, *10*, 1155–1169, doi:10.5194/acp-10-1155-2010.

649 Sano, I., S. Mukai, Y. Okada, B. N. Holben, S. Ohta, and T. Takamura (2003), Optical properties
650   of aerosols during APEX and ACE-Asia experiments, *J. Geophys. Res.*, *108*(D23), 8649,
651   doi:10.1029/2002JD003263.

652 Satheesh, S. K., K. K. Moorthy (2005), Radiative effects of natural aerosols: A review, *Atmos.*
653   *Environ.*, *39*, 11, 2089-2110, doi:10.1016/j.atmosenv.2004.12.029.

654 Schafer, J. S., T. F. Eck, B. N. Holben, P. Artaxo, and A. F. Duarte (2008), Characterization of
655   the optical properties of atmospheric aerosols in Amazônia from long-term AERONET
656   monitoring (1993–1995 and 1999–2006), *J. Geophys. Res.*, *113*, D04204,
657   doi:10.1029/2007JD009319.

658 Singh, R. P., S. Dey, S. N. Tripathi, V. Tare, and B. Holben (2004), Variability of aerosol
659   parameters over Kanpur, northern India, *J. Geophys. Res.*, *109*, D23206,
660   doi:10.1029/2004JD004966.

661 Smirnov, A., B. N. Holben, T. F. Eck, O. Dubovik, and I. Slutsker (2000), Cloud-screening and
662   quality control algorithms for the AERONET database, *Remote Sens. Environ.*, *73*, 337–
663   349, doi:10.1016/S0034-4257(00) 00109-7.

664 Smirnov, A., B. N. Holben, Y. J. Kaufman, O. Dubovik, T. F. Eck, I. Slutsker, C. Pietras, R. N.
665   Halthore (2002), Optical Properties of Atmospheric Aerosol in Maritime Environments.
666   *J. Atmos. Sci.*, *59*, doi: 10.1175/1520-0469(2002)059<0501:OPOAAI>2.0.CO;2.

667 Smirnov, A., et al. (2009), Maritime Aerosol Network as a component of Aerosol Robotic
668   Network, *J. Geophys. Res.*, *114*, D06204, doi:10.1029/2008JD011257.

669 Sokolik, I. N., and O. B. Toon (1999), Incorporation of mineralogical composition into models
670   of the radiative properties of mineral aerosol from UV to IR wavelengths, *J. Geophys.*
671   *Res.*, 104(D8), 9423–9444, doi:10.1029/1998JD200048.

672 Tanré, D., Y. J. Kaufman, B. N. Holben, B. Chatenet, A. Karnieli, F. Lavenu, L. Blarel, O.
673   Dubovik, L. A. Remer, and A. Smirnov (2001), Climatology of dust aerosol size
674   distribution and optical properties derived from remotely sensed data in the solar
675   spectrum, *J. Geophys. Res.*, *106*, 18,205–18,217, doi:10.1029/2000JD900663.

676 Toledano, C., et al. (2011), Optical properties of aerosol mixtures derived from sun-sky
677   radiometry during SAMUM-2, *Tellus*, Ser. B, *63*, 635–648, doi:10.1111/j.1600-
678   0889.2011.00573.x.

679 Voronoi, G. F. (1908). Nouvelles applications des parametres continus aÂ la theÂorie de forms
680   quadratiques, *J. Reine Agnew. Math.*, *134*, 198-287.

681 Yang, M., Howell, S. G., Zhuang, J., and Huebert, B. J. (2009), Attribution of aerosol light
682   absorption to black carbon, brown carbon, and dust in China – interpretations of
683   atmospheric measurements during EAST-AIRE, *Atmos. Chem. Phys.*, *9*, doi:10.5194/acp-
684   9-2035-2009.

685

686 **Table 1.** Previous studies identifying regional aerosol sources affecting AERONET sites

Aerosol Type Source Regions	Affected AERONET Sites	Selected References
Most Regions with Various Types	Most Sites	*Holben et al.* [2001]
Dust - African	Banizoumbou, Capo Verde, Dakar, Ouagadougou,	*Tanre et al.* [2001]; *Reid et al.* [2003]
Dust - Asian	XiangHe, Shirahama	*Eck et al.* [2005]
Smoke -Amazonia	Abracos Hill, Alta Floresta	*Eck et al.* [2003b]; *Schafer et al.* [2008]
Smoke - Australian	Lake_Argyle	*Mitchell et al.* [2006]
Smoke - Boreal	Bonanza Creek	*Eck et al.* [2009]
Smoke - African	Mongu	*Eck et al.* [2003a; 2003b]
Pollution - Europe	Ispra	*Melin and Zibordi* [2005]
Mixed - Asia	XiangHe, SEDE_BOKER	*Derimian et al.* [2006]; *Eck et al.* [2010]; *Yang et al.* [2009]
Mixed - India	Kanpur	*Dey et al.* [2004]; *Singh et al.* [2004]; *Prasad et al.* [2007]; *Giles et al.* [2011a]
Mixed - Africa	Ilorin	*Eck et al.* [2010]

Table 2. Average aerosol absorption and size properties by aerosol type category from AERONET Version 2 almucantar retrievals[a]

Site	Date Range	ω_o 440/675/870/1020 nm	$\alpha_{abs440-870nm}$	$\alpha_{ext440-870nm}$	η_{550nm}	N
		Dust				
Banizoumbou	1999-2010	0.91/0.95/0.96/0.96 0.04/0.04/0.04/0.04	1.7±0.6	0.3±0.2	0.28±0.20	2901
Capo_Verde	1999-2010	0.91/0.96/0.97/0.97 0.03/0.03/0.03/0.03	2.0±0.6	0.2±0.2	0.24±0.16	1202
Dakar	2000-2010	0.89/0.95/0.96/0.96 0.03/0.04/0.04/0.03	1.9±0.6	0.3±0.2	0.28±0.23	2250
Ouagadougou	1999-2007	0.90/0.94/0.95/0.95 0.04/0.04/0.04/0.03	1.6±0.5	0.3±0.2	0.30±0.21	1497
Solar_Village	1999-2010	0.91/0.95/0.96/0.96 0.02/0.02/0.02/0.02	1.8±0.6	0.3±0.3	0.28±0.25	3029
		Mixed (for $0.33<\eta_{550nm}\leq0.66$)				
Ilorin	1999-2009	0.86/0.90/0.92/0.92 0.05/0.05/0.04/0.04	1.6±0.4	0.7±0.2	0.47±0.23	798
Kanpur	2001-2010	0.87/0.90/0.92/0.93 0.03/0.03/0.03/0.03	1.4±0.4	0.7±0.2	0.48±0.22	963
SEDE_BOKER	1999-2010	0.91/0.93/0.93/0.94 0.02/0.02/0.03/0.03	1.2±0.5	0.7±0.2	0.48±0.20	170
XiangHe	2001, 2004-2010	0.88/0.92/0.93/0.93 0.03/0.03/0.03/0.03	1.8±0.4	0.8±0.2	0.53±0.22	446

688   [a] Aerosol optical depth (AOD) at 440 nm is greater than 0.4 for Version 2, Level 2.0 almucantar retrievals. The spectral single
689   scattering albedo (ω_o) averages are listed first followed by their standard deviations. The absorption and extinction Ångström
690   exponents (α_{abs} and α_{ext}) and are computed using the 440-675-870 nm wavelength interval. The fine mode fraction of the AOD
691   (η_{550nm}) is interpolated to 550 nm as discussed in Section 2.

692

693

Table 2. (Continued)

Site	Date Range	ω_o 440/675/870/1020 nm	$\alpha_{abs440-870nm}$	$\alpha_{ext440-870nm}$	η_{550nm}	N
Urban/Industrial					
GSFC	1999–2010	0.96/0.95/0.94/0.93 0.02/0.02/0.03/0.03	1.1±0.2	1.8±0.2	0.94±0.20	882
Ispra	1999-2010	0.93/0.93/0.92/0.91 0.03/0.04/0.04/0.04	1.4±0.4	1.6±0.2	0.92±0.24	583
Mexico_City	1999-2010	0.89/0.88/0.86/0.85 0.04/0.04/0.05/0.06	1.3±0.3	1.6±0.2	0.87±0.18	540
Moldova	1999-2010	0.93/0.92/0.90/0.89 0.03/0.04/0.05/0.05	1.2±0.3	1.6±0.3	0.87±0.28	558
Shirahama	2000-2010	0.94/0.93/0.92/0.92 0.03/0.03/0.04/0.05	1.1±0.5	1.3±0.3	0.81±0.35	726
Biomass Burning					
Abracos_Hill	1999-2005	0.93/0.91/0.90/0.88 0.02/0.03/0.04/0.05	1.3±0.4	2.0±0.1	0.95±0.14	342
Alta_Floresta	1999-2010	0.93/0.92/0.90/0.89 0.02/0.03/0.04/0.05	1.5±0.4	1.9±0.2	0.92±0.18	593
Bonanaza Creek	1999-2005, 2008-2010	0.95/0.96/0.96/0.95 0.03/0.03/0.04/0.04	1.8±0.5	1.5±0.2	0.96±0.22	144
Lake_Argyle	2002-2006, 2009-2010	0.85/0.83/0.82/0.81 0.04/0.05/0.06/0.07	1.4±0.3	1.5±0.4	0.79±0.36	176
Mongu	1999-2007, 2009	0.87/0.83/0.80/0.77 0.03/0.04/0.04/0.05	1.2±0.2	1.9±0.1	0.92±0.10	1411

694

30

| Type	λ (nm)	$\dfrac{\alpha_{abs}{}^{a}}{\delta\omega_o=0.0}$	$\delta\omega_o$	$\delta\alpha_{abs}{}^{b}$ All $\tau(\lambda)$	τ_{440nm}	τ_{870nm}	N
Dust	440-675-870	1.76±0.58	-0.01	-0.27			10879
		1.67±0.52	+0.01^c	+0.40			9807
		1.76±0.58	-0.02	-0.45			10879
		1.49±0.42	+0.02^c	+0.67			7290
		1.76±0.58	-0.03^d	-0.57	+0.47	-0.90	10879
		1.33±0.38	+0.03^{cd}	+0.79	-0.54	+1.16	4898
		1.76±0.58	-0.04	-0.67			10879
		1.23±0.36	+0.04^c	+0.85			3342
Mixed	440-675-870	1.53±0.44	-0.01	-0.09			7199
		1.52±0.42	+0.01^c	+0.13			7051
		1.53±0.44	-0.02	-0.16			7199
		1.47±0.38	+0.02^c	+0.23			6623
		1.53±0.44	-0.03^d	-0.21	+0.40	-0.53	7199
		1.43±0.35	+0.03^{cd}	+0.30	-0.51	+0.71	6060
		1.53±0.44	-0.04	-0.25			7199
		1.40±0.33	+0.04^c	+0.35			5479
Urban/ Industrial	440-675-870	1.21±0.37	-0.01	+0.05			3289
		1.20±0.36	+0.01^c	-0.10			3174
		1.21±0.37	-0.02	+0.09			3289
		1.19±0.35	+0.02^c	-0.21			2874
		1.21±0.37	-0.03^d	+0.12	+0.74	-0.52	3289
		1.18±0.34	+0.03^{cd}	-0.31	-1.02	+0.58	2428
		1.21±0.37	-0.04	+0.14			3289
		1.18±0.34	+0.04^c	-0.40			2027
Biomass Burning	440-675-870	1.35±0.35	-0.01	+0.03			2666
		1.34±0.34	+0.01^c	-0.04			2639
		1.35±0.35	-0.02	+0.06			2666
		1.33±0.32	+0.02^c	-0.10			2598
		1.35±0.35	-0.03^d	+0.08	+0.45	-0.31	2666
		1.32±0.31	+0.03^{cd}	-0.19	-0.62	+0.35	2512
		1.35±0.35	-0.04	+0.11			2666
		1.31±0.29	+0.04^c	-0.29			2421

697   ^{a} indicates the unperturbed α_{abs} average is recalculated based on available ω_o.

698   ^{b} indicates wavelength(s) used in perturbation of ω_o.

699   ^{c} indicates positive perturbation of ω_o must be less than 0.995 for any wavelength.

700   ^{d} indicates these criteria are the current uncertainty estimates based on *Dubovik et al.* [2000].

701

702
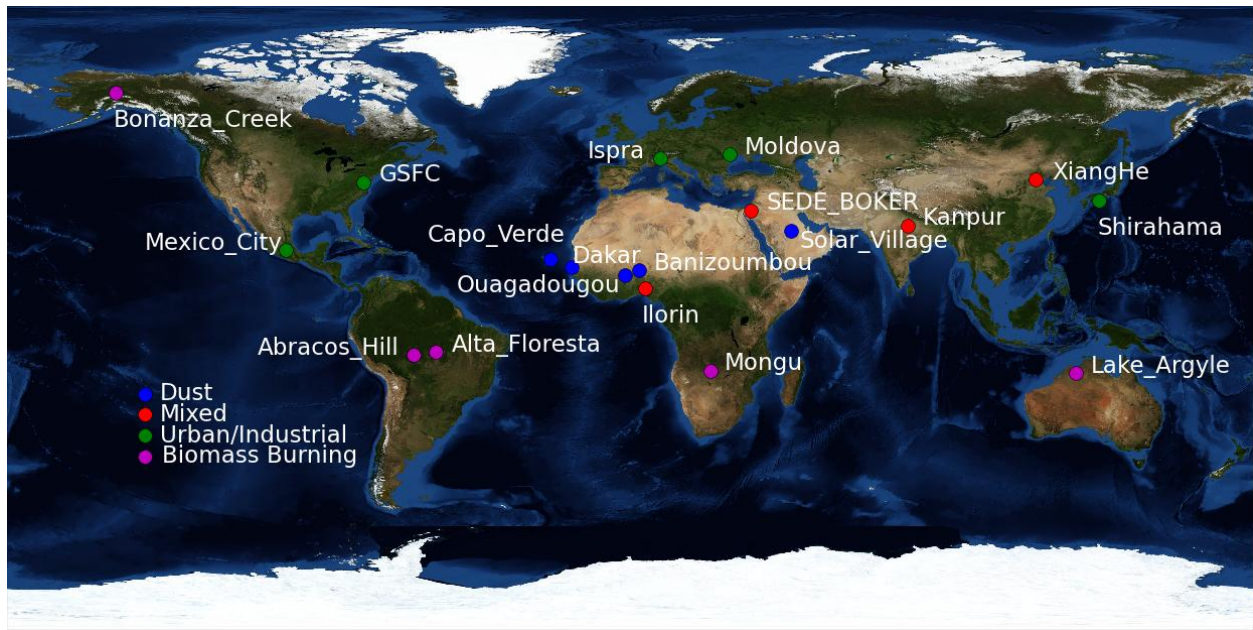
Figure 1. Distribution of the AERONET sites based on the dominant particle type. Sites were selected based on data volume, geographic location, and primary aerosol source region. Other dominant particle types (e.g., sea salt and biogenic aerosols) were not considered due to low aerosol loading conditions ($\tau_{440nm} \leq 0.4$), which was a limiting threshold for AERONET Version 2, Level 2.0 aerosol absorption retrievals [*Dubovik et al.*, 2002; *Holben et al.*, 2006].
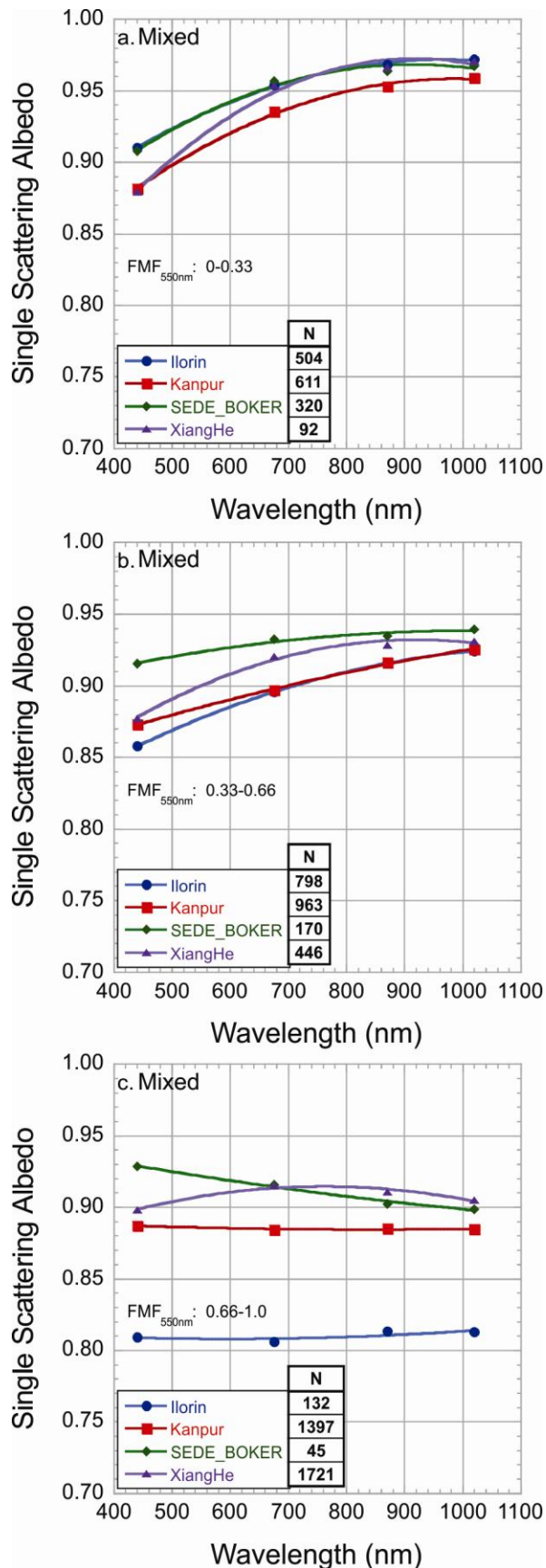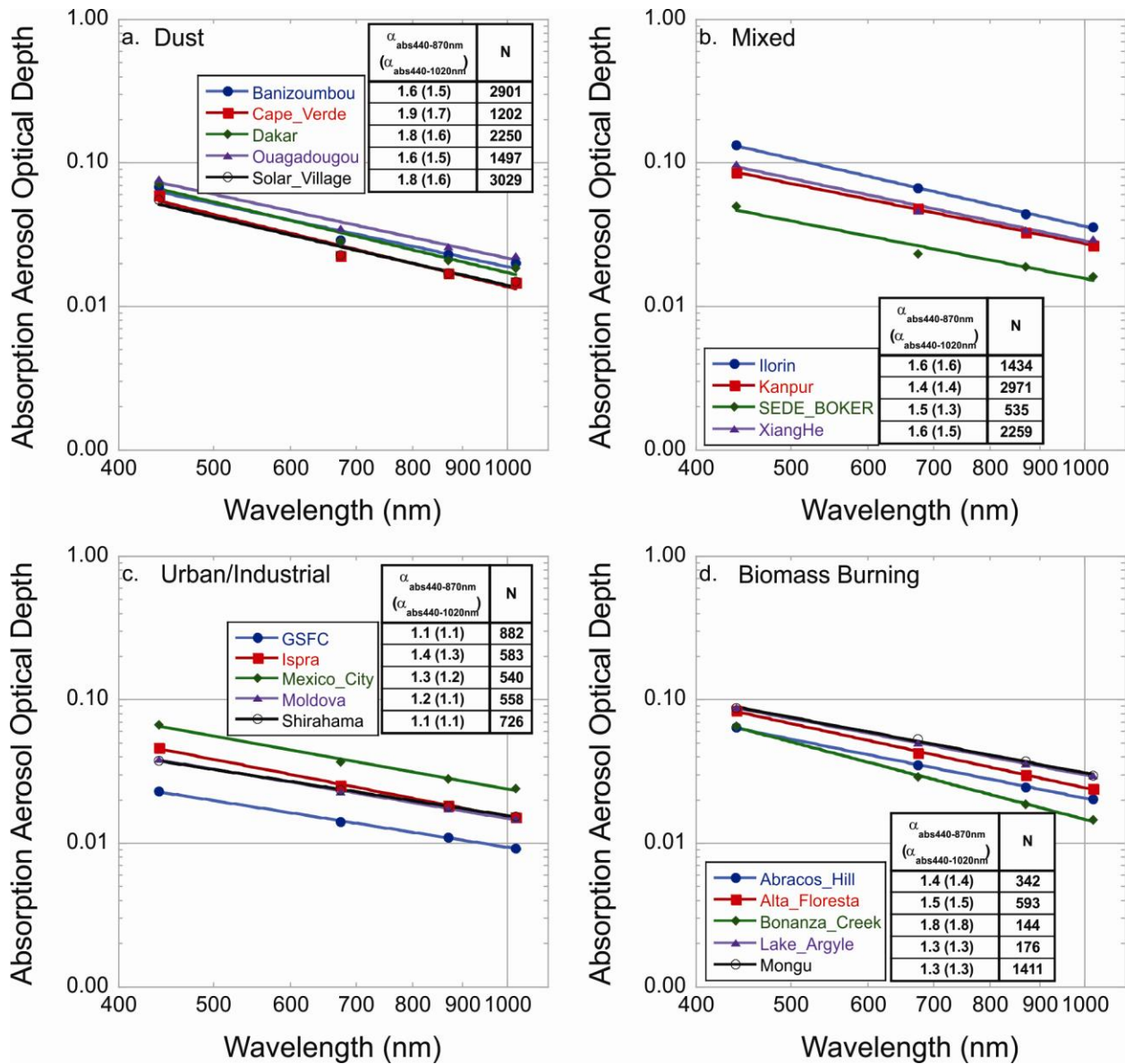
708
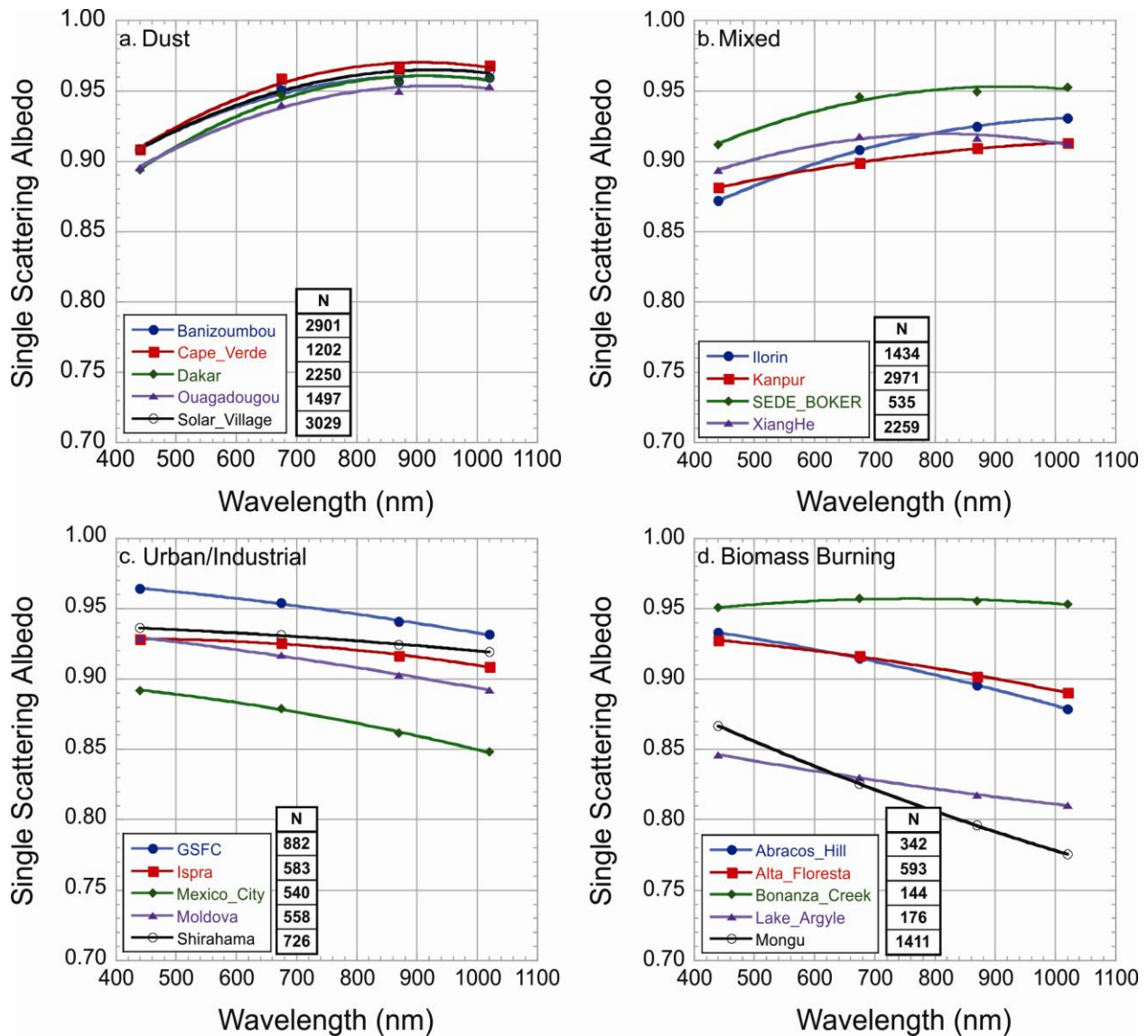
Figure 2. Spectral single scattering albedo averages were grouped by dominant aerosol particle category for $\tau_{440nm}>0.4$ using AERONET Version 2, Level 2.0 data. The plots utilize second order polynomial fit.
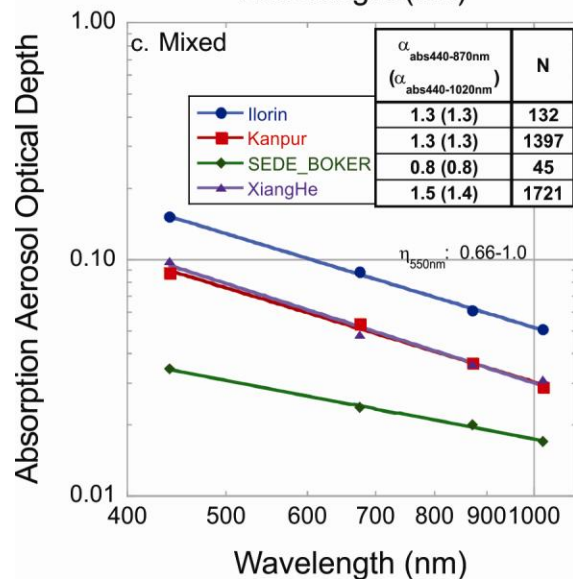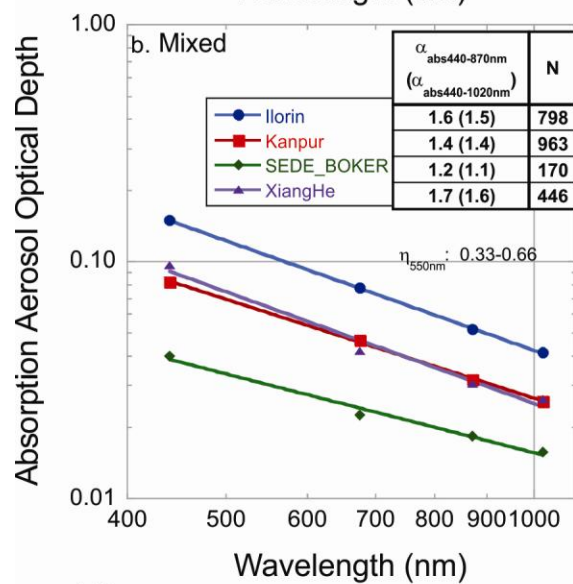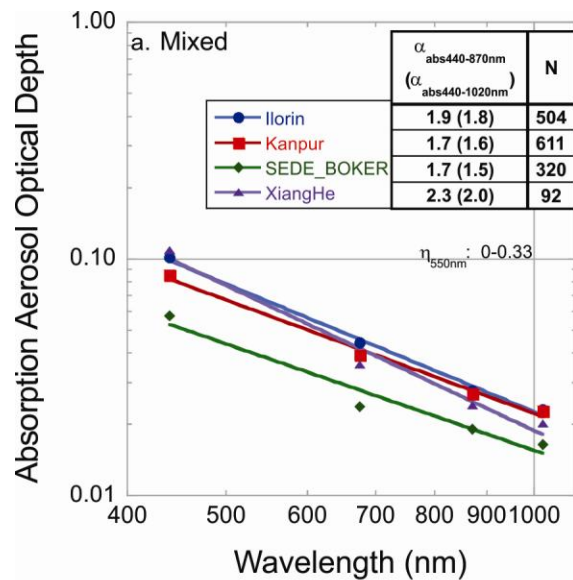
Figure 3. Similar to Figure 2, except the spectral single scattering albedo averages for the Mixed category were grouped by fine mode fraction of AOD (η_{550nm}) using the ranges 0.0-0.33 for coarse mode dominated particles (a), 0.33-0.66 for mixed size particles (b), and 0.66-1.0 for fine mode dominated particles (c).

a. Dust

	$\alpha_{abs440-870nm}$ ($\alpha_{abs440-1020nm}$)	N
Banizoumbou	1.6 (1.5)	2901
Cape_Verde	1.9 (1.7)	1202
Dakar	1.8 (1.6)	2250
Ouagadougou	1.6 (1.5)	1497
Solar_Village	1.8 (1.6)	3029

b. Mixed

	$\alpha_{abs440-870nm}$ ($\alpha_{abs440-1020nm}$)	N
Ilorin	1.6 (1.6)	1434
Kanpur	1.4 (1.4)	2971
SEDE_BOKER	1.5 (1.3)	535
XiangHe	1.6 (1.5)	2259

c. Urban/Industrial

	$\alpha_{abs440-870nm}$ ($\alpha_{abs440-1020nm}$)	N
GSFC	1.1 (1.1)	882
Ispra	1.4 (1.3)	583
Mexico_City	1.3 (1.2)	540
Moldova	1.2 (1.1)	558
Shirahama	1.1 (1.1)	726

d. Biomass Burning

	$\alpha_{abs440-870nm}$ ($\alpha_{abs440-1020nm}$)	N
Abracos_Hill	1.4 (1.4)	342
Alta_Floresta	1.5 (1.5)	593
Bonanza_Creek	1.8 (1.8)	144
Lake_Argyle	1.3 (1.3)	176
Mongu	1.3 (1.3)	1411

Figure 4. Absorption aerosol optical depth (τ_{abs}) and absorption Ångström exponent (α_{abs}) averages were grouped by dominant aerosol particle category for $\tau_{440nm}>0.4$ using AERONET Version 2, Level 2.0 data. The plots use the power law fit and slopes of these lines are the α_{abs} (440-870 nm or 440-1020 nm) listed adjacent to the legend in each plot.

35

a. Mixed

$\alpha_{abs440-870nm}$ ($\alpha_{abs440-1020nm}$)	N
Ilorin		
1.9 (1.8)	504
Kanpur		
1.7 (1.6)	611
SEDE_BOKER		
1.7 (1.5)	320
XiangHe		
2.3 (2.0)	92

η_{550nm}: 0-0.33

Absorption Aerosol Optical Depth

Wavelength (nm)

b. Mixed

$\alpha_{abs440-870nm}$ ($\alpha_{abs440-1020nm}$)	N
Ilorin		
1.6 (1.5)	798
Kanpur		
1.4 (1.4)	963
SEDE_BOKER		
1.2 (1.1)	170
XiangHe		
1.7 (1.6)	446

η_{550nm}: 0.33-0.66

Absorption Aerosol Optical Depth

Wavelength (nm)

c. Mixed

$\alpha_{abs440-870nm}$ ($\alpha_{abs440-1020nm}$)	N
Ilorin		
1.3 (1.3)	132
Kanpur		
1.3 (1.3)	1397
SEDE_BOKER		
0.8 (0.8)	45
XiangHe		
1.5 (1.4)	1721

η_{550nm}: 0.66-1.0

Absorption Aerosol Optical Depth

Wavelength (nm)

Figure 5. Similar to Figure 3, except τ_{abs} and α_{abs} averages for the Mixed category were grouped by fine mode fraction of the AOD (η_{550nm}) using ranges of 0.0-0.33 for coarse mode dominated particles (a), 0.33-0.66 for mixed size particles (b), and 0.66-1.0 for fine mode particles (c).
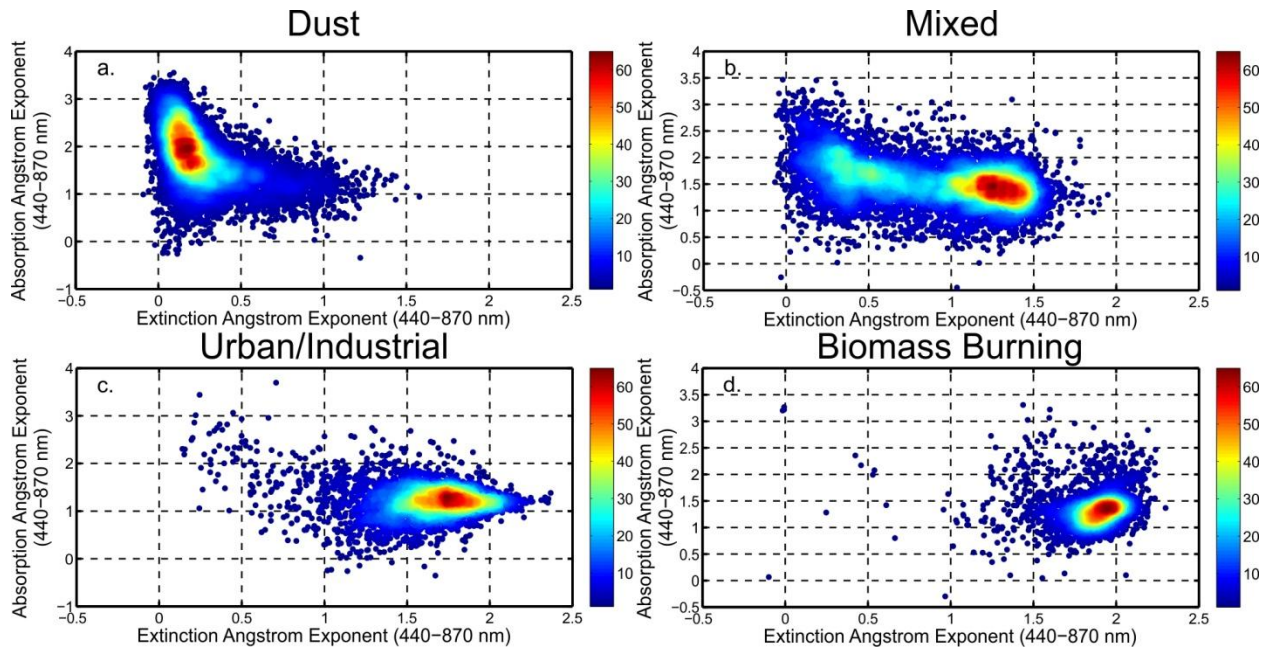
737
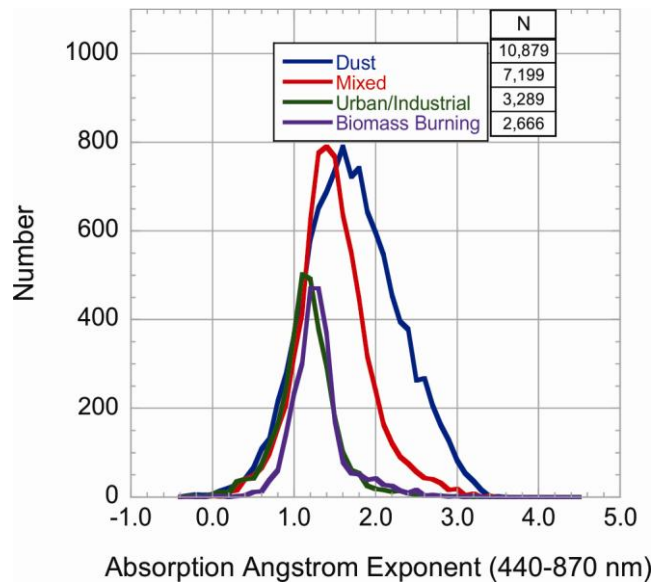
Figure 6. Absorption Ångström exponent (α_{abs}) frequency distribution for each dominant
aerosol particle category using AERONET Version 2, Level 2.0 data. Approximately 10% of the
α_{abs} retrievals (22% for Urban/Industrial) were below 1.0 or λ^{-1} dependence.

741

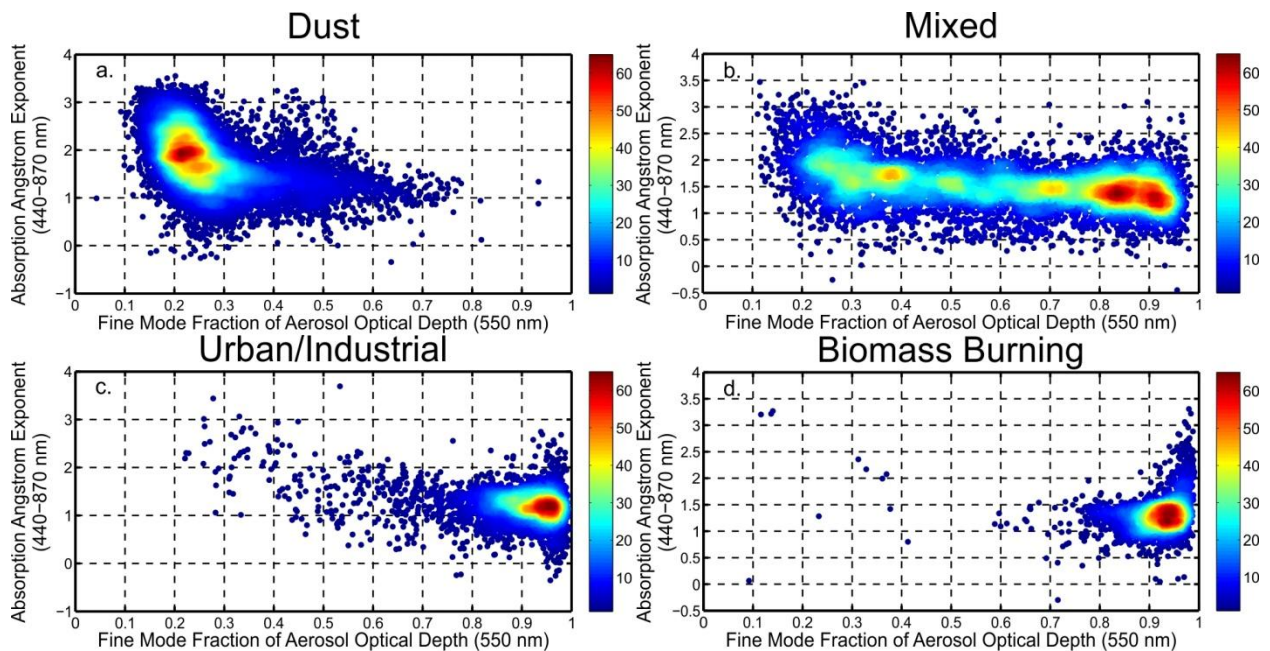**Figure 7.** Relative number density plots for the absorption Ångström exponent (440-870 nm) and extinction Ångström exponent (440-870 nm) relationship based on dominant aerosol type using AERONET Version 2, Level 2.0 data. The color scale represents the relative density of points in each aerosol type partitioned data set, where orange to red colors (levels ~45-64) indicate the highest number density based on the Voronoi tessellation.
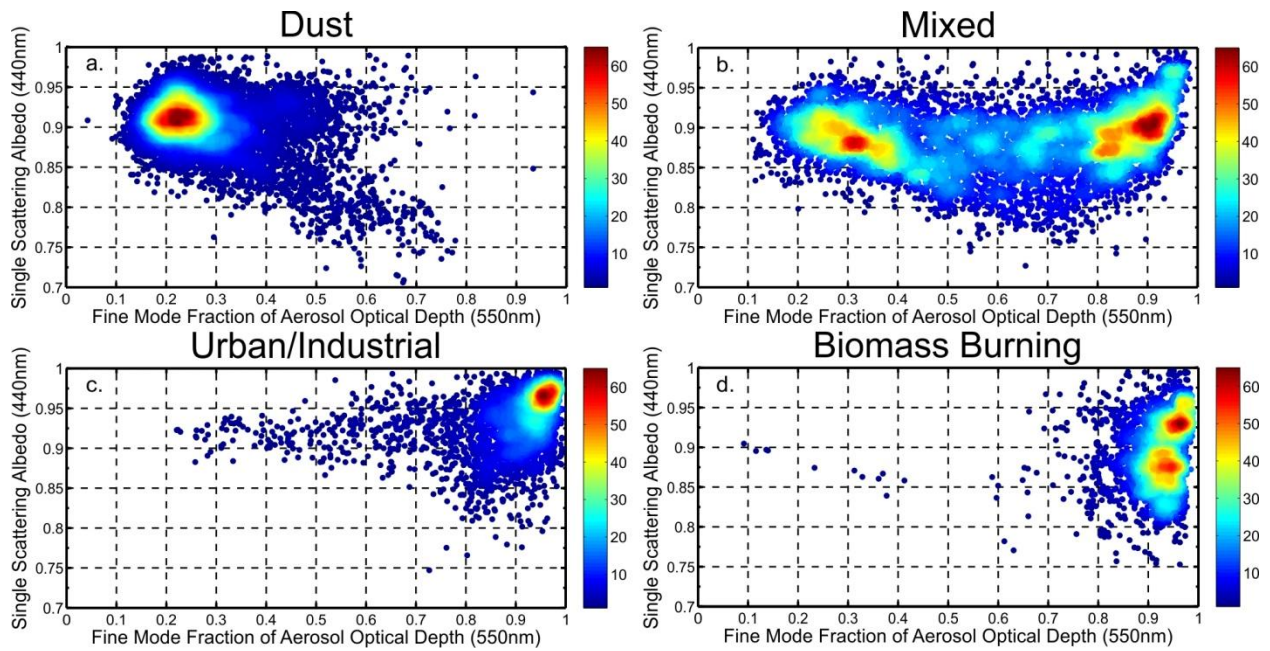

Figure 8. Similar to Figure 7, except for the absorption Ångström exponent (440-870 nm) and fine mode fraction of the aerosol optical depth (550 nm) relationship.
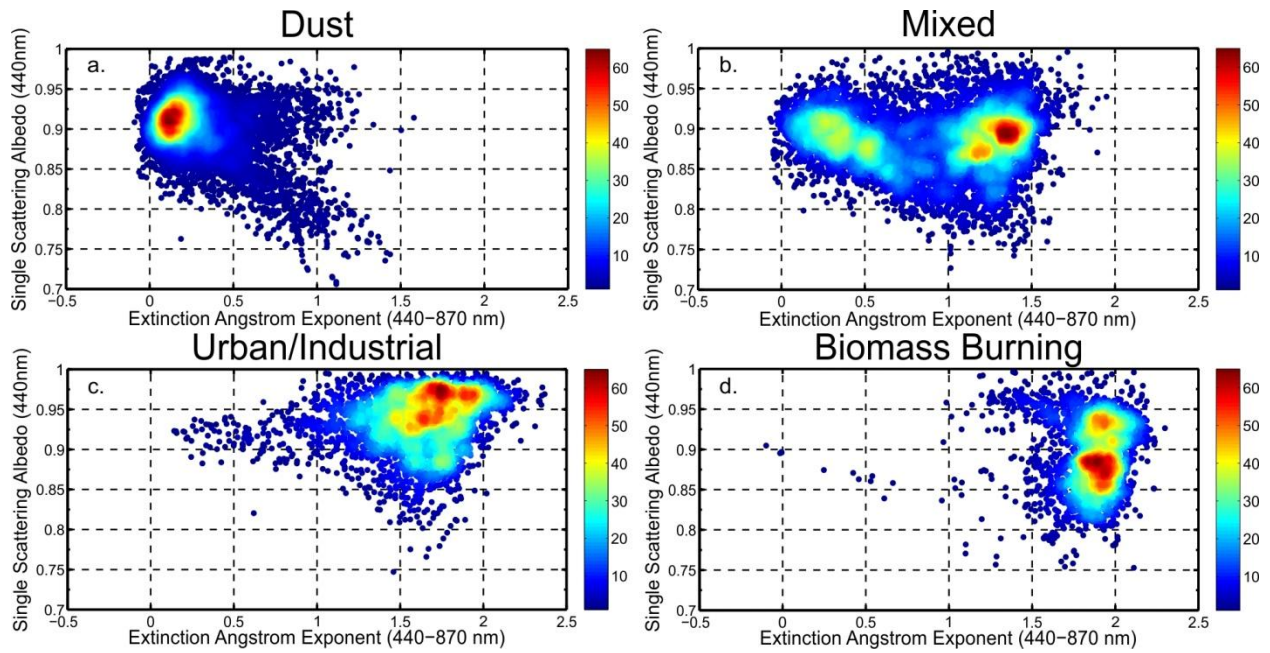
Figure 9. Similar to Figure 7, except for the single scattering albedo (440 nm) and the extinction Ångström exponent (440-870 nm) relationship.
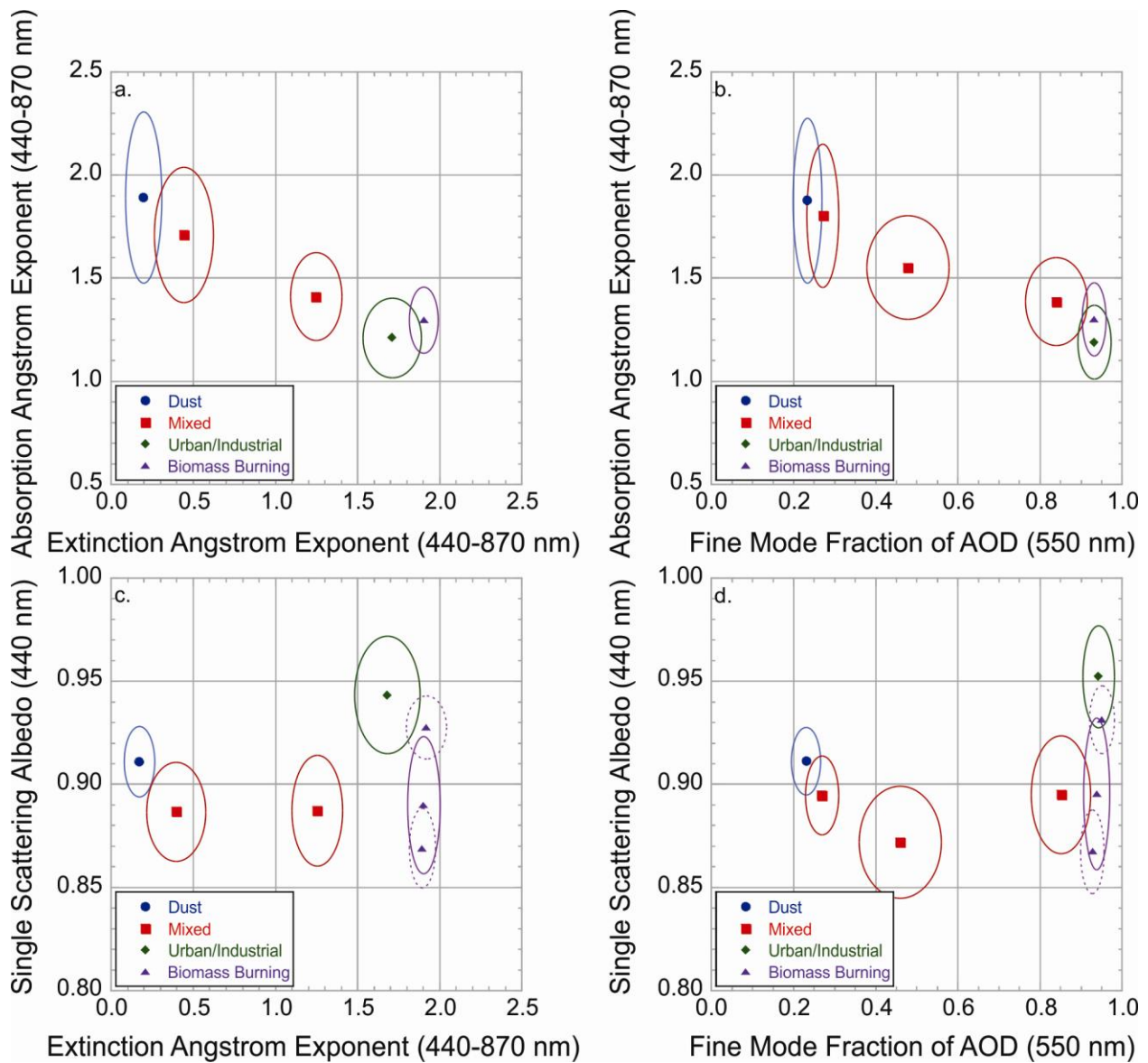

Figure 10. Similar to Figure 7, except for the single scattering albedo (440 nm) and fine mode fraction of the aerosol optical depth (550 nm) relationship.

Figure 11. Weighted cluster averages were grouped for each aerosol type category and relationship using AERONET Version 2, Level 2.0 data. The Mixed category averages were calculated using a 0.8 extinction Ångström exponent threshold between mainly small and mainly large particles. For the fine mode fraction of AOD, the Mixed category averages were calculated based on the 0.0-0.33, 0.33-0.66, and 0.66-1.0 ranges. For single scattering albedo plots, the Biomass Burning category was further partitioned by calculating averages using a single scattering albedo threshold of 0.90 to produce two sub-clusters (dashed ellipses) observed in Figure 9 and Figure 10.